AD-A160 011   FUNDAMENTAL PROCESSES IN PARTIALLY IONIZED PLASMAS(U)   1/1
               STANFORD UNIV CA HIGH TEMPERATURE GASDYNAMICS LAB
               C H KRUGER ET AL. MAR 85 AFOSR-TR-85-0811 AFOSR-83-0108
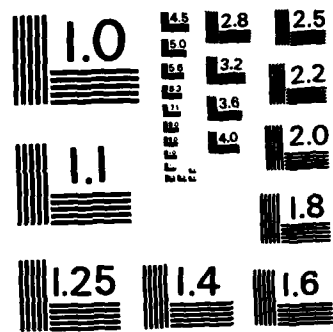UNCLASSIFIED   F/G 20/9   NL

END
FILMED
DTIC

MICROCOPY RESOLUTION TEST CHART

NATIONAL BUREAU OF STANDARDS-1963-A

AFOSR-TR- 0 5 .081 :

②

Annual Scientific Report

on

FUNDAMENTAL PROCESSES IN PARTIALLY IONIZED PLASMAS

Grant AFOSR-83-0108

Prepared for

AIR FORCE OFFICE OF SCIENTIFIC RESEARCH

For the Period

February 1, 1984 to January 31, 1985

DTIC
ELECTE
OCT 1 1 1985
S B

Submitted by

C. H. Kruger, Principal Investigator
M. Mitchner, Co-Principal Investigator
S. A. Self, Co-Principal Investigator

HIGH TEMPERATURE GASDYNAMICS LABORATORY
Mechanical Engineering Department
Stanford University

85 10 11 086

Annual Scientific Report

on

FUNDAMENTAL PROCESSES IN PARTIALLY IONIZED PLASMAS

Grant AFOSR-83-0108

Prepared for

AIR FORCE OFFICE OF SCIENTIFIC RESEARCH

For the Period

February 1, 1984 to January 31, 1985

Submitted by

C. H. Kruger, Principal Investigator
M. Mitchner, Co-Principal Investigator
S. A. Self, Co-Principal Investigator

REPORT DOCUMENTATION PAGE	READ INSTRUCTIONS BEFORE COMPLETING FORM

1. REPORT NUMBER	2. GOVT ACCESSION NO.	3. RECIPIENT'S CATALOG NUMBER
AFOSR-TR- 85-0811	AD-A160 011	

4. TITLE (and Subtitle)	5. TYPE OF REPORT & PERIOD COVERED
Fundamental Processes in Partially Ionized Plasmas	Annual Scientific Report Feb. 1, 1984 to Jan. 31, 1985
	6. PERFORMING ORG. REPORT NUMBER

7. AUTHOR(s)	8. CONTRACT OR GRANT NUMBER(s)
C. H. Kruger, Principal Investigator M. Mitchner, Co-Principal Investigator S.A. Self, Co-Principal Investigator	Grant AFOSR-83-0108

9. PERFORMING ORGANIZATION NAME AND ADDRESS	10. PROGRAM ELEMENT, PROJECT, TASK AREA & WORK UNIT NUMBERS
Stanford University Mechanical Engineering Department Stanford, California 94305	61102F 2301/A1

11. CONTROLLING OFFICE NAME AND ADDRESS	12. REPORT DATE
Major Henry L. Pugh, Jr., Major, USAF Program Manager, Directorate of Physical & Geo Sci	March 1985
AFOSR/NP, Bolling AFB, Building 410, Wash. D.C.	13. NUMBER OF PAGES

14. MONITORING AGENCY NAME & ADDRESS(if different from Controlling Office)	15. SECURITY CLASS. (of this report)
	Unclassified
	15a. DECLASSIFICATION/DOWNGRADING SCHEDULE N/A

16. DISTRIBUTION STATEMENT (of this Report)

Approved for public release;
distribution unlimited.

17. DISTRIBUTION STATEMENT (of the abstract entered in Block 20, if different from Report)

18. SUPPLEMENTARY NOTES

19. KEY WORDS (Continue on reverse side if necessary and identify by block number)

Plasma	Sheath	Secondary flow	Turbulence-dampening
Ionized	Weakly-ionized	Power	Anode
Recombination	Boundary layer	Hartmann	Cathode
Three-body	Magnetohydrodynamic	Diagnostics	Electrothermal
Discharge	MHD	Propulsion	Breakdown

20. ABSTRACT (Continue on reverse side if necessary and identify by block number)

This report describes progress during the second year of a research program on the Fundamental Processes in Partially Ionized Plasmas conducted in the High Temperature Gasdynamics Laboratory at Stanford University. This research is directed to three major areas: recombination in molecular plasmas, discharge effects (plasma electrode interaction) and interaction of discharges and fluid dynamics. Recombination and ionization are fundamental processes that play a role in nearly all applications and natural phenomena that involve partially ionized plasmas. Under the present program, experiments have been designed

DD FORM 1473   EDITION OF 1 NOV 65 IS OBSOLETE
1 JAN 73

BLOCK 20 (Abstract)

and theoretical analyses conducted to obtain a better knowledge of the rates of electron recombination in the presence of molecular species. Studies are continuing of the near-electrode region and the processes by which current is transferred between the plasmas and the electrodes. The first stage of theoretical modeling of these processes has now been completed and published. A study of the interaction of discharges and fluid dynamics has measured the significant secondary flows caused by the interaction of a magnetic field with a current-carrying plasma. Measurements have been made of secondary flows, and of their effects on profiles of axial velocity, turbulence intensity and electrical conductivity. Experimental and theoretical research in each of these areas is continuing.

Table of Contents

1.0 INTRODUCTION

This report describes progress during the second year of a research program on the Fundamental Processes in Partially Ionized Plasmas conducted in the High Temperature Gasdynamics Laboratory at Stanford University. This research is supported by a grant from the Air Force Office of Scientific Research (AFOSR-83-0108) and is conducted under the direction of Professors Charles H. Kruger, Morton Mitchner, and Sidney Self. Three Ph.D. candidates are currently conducting their doctoral research under this program.

Several space power and propulsion systems of potential long-range interest to the Air Force involve partially ionized plasmas. Such systems include MPD thrusters, both open and closed cycle MHD power, and thermionic energy conversion. Although the specific configurations, the exact operating conditions, and which of the competing systems will prove to be most useful in the long term remain to be established, it is important at this time to provide a broad fundamental research base in support of development activity. In particular, there are a number of key issues regarding the properties and discharge behavior of partially ionized plasmas and the interaction of discharges with fluid dynamics that need to be understood before the potential and limitations of competing systems can be fully evaluated. In addition, it is important that outstanding young applied scientists be educated in these areas.

The present research on partially ionized plasmas is discipline rather than device oriented and is currently focused on three major areas:

1. Recombination in molecular plasmas

2. Discharge effects: plasma electrode interaction

3. Interaction of discharges and fluid dynamics

In addition, each of these areas involves the development and application of modern plasma diagnostic techniques.

These areas are overlapping and mutually supportive. Thus, understanding of plasma properties is important to the study of discharges and their interaction with fluid dynamics. In the same spirit, we are interested in the development of plasma diagnostics so that they can be applied in our research objectives. In each area, the research is primarily experimental in nature, with supporting theoretical studies for the planning of the research and interpretation of the data.

Progress during the second year in each of the three research areas is described by means of Project Summaries in Section 2.0.

Publications and Presentations resulting from this work are cited in Section 4.0, and Section 5.0 lists the personnel who have contributed to this report.

2.0 PROJECT SUMMARIES

Included in this section are summaries of progress in each of three project areas. Each project summary contains the following subsections: (a) Introduction; (b) Research Objectives; and (c) Status of Research. Additional descriptions may be found in the publications listed in Section 4.0.

2.1 Recombination in Molecular Plasmas

Introduction

The goal of this study is to make measurements of the 3-body electron recombination coefficient $\alpha_k(T)$ for the process $e + M^+ + X_k \rightarrow M + X_k$, and to compare experimental data with recent theoretical results. Here e denotes an electron, M and M^+ denote an atom and an ion respectively of an alkali metal, and X_k is a molecular species. In particular, initial considerations have been focused on the alkali metal Cs and on the molecule N_2. This work is motivated in part by measurements of appreciable electron-density nonequilibrium in plasma boundary layers that cannot be adequately explained by existing data for known recombination processes [1.1]. Such boundary layers can exist in devices that have been proposed for generating electrical power in space (and could exist also in some space propulsion applications).

The recombination of an electron e with an alkali metal ion M^+ by one or both of the two 3-body processes

$$e + M^+ + e \rightarrow M + e \qquad (1.1)$$

$$e + M^+ + X_k \rightarrow M + e \qquad (1.2)$$

plays an important role in many applications that involve the nonequilibrium behavior of partially ionized gases. In the first process, the third body (which is required in order to conserve momentum and energy) is an electron; in the second process, the third body is an atom or a molecule X_k. In this work, the temperature dependent recombination rate coefficients for the two processes, $\alpha_e(T)$ and $\alpha_k(T)$, are defined by the relations

$$\frac{dn_e}{dt} = -\alpha_e n_e^2 n_i \qquad (1.3)$$

$$\frac{dn_e}{dt} = -\alpha_k n_k n_e n_i \qquad (1.4)$$

where n_i is the number density (cm^{-3}) of ions and t is time (sec).

Experimental studies of the recombination process in which the third body is an atom or molecule have been carried out using (hydrocarbon) flames [1.2], where the products of combustion contained several molecular species. To extract information about the individual molecules X_j, the assumption was made that the contributions from the different molecules in the mixture were additive. Expressed equivalently, in terms of recombination coefficients, it was assumed that the overall rate α (which was measured, in effect) could be written in terms of the individual rates α_j by the formula

$$\alpha = \sum_j x_j \alpha_j \quad ,$$

where $x_j = n_j/n$ denotes the mole fraction of species X_j. Here n_j is the number density of species X_j and n is the total number density.

The results obtained in this fashion have been strongly criticized by Bates [1.3], who claimed that the recombination coefficient for a molecular mixture is <u>not additive</u>, but that it is given by the formula

$$\alpha = \frac{n}{\eta} \left\{ \sum_p \frac{1}{\sum_j x_j B_j(p)} \right\}^{-1} .$$

The quantities $B_j(p)$ are related to the rates of de-excitation of M by X_j from all energy levels above and including p, to all levels below p. The factor η is given in terms of atomic constants and the temperature T as $(2\pi m_e kT/h^2)^{3/2} = KT^{3/2}$.

For a single species, one obtains from this expresison for α the result

$$\alpha_j = \frac{n_j}{\eta} \left\{ \sum_p \frac{1}{B_j(p)} \right\}^{-1} .$$

- 4 -

It is therefore apparent that the value of α for a mixture of molecules cannot be written, in general, in terms of the individual α_j. To be able to calculate α for a mixture, the factors $B_j(p)$ must be used. However before being able to rely on the calculated factors $B_j(p)$, it is necessary to test the theory by obtaining data in which only a single molecular species X_j is present in the recombining gas together with the alkali metal M. It is clear that flame experiments are unable to yield such data.

Research Objectives

1. To design and construct an experimental system that can produce a recombining alkali metal plasma under conditions where the molecular three-body process dominates.

2. To examine, in particular, the recombination of cesium ions in the presence of nitrogen.

3. To measure the desired recombination rate as a function of the background gas temperature.

4. To measure the recombination rate as a function of various values of the partial pressures of Cs and N_2.

5. To examine the recombination rate of interest in a mixture of molecular species.

6. To design and construct a suitable pulse forming circuit for a high intensity flashlamp and to explore the use of pulsed photoionization as a means for producing the desired plasma conditions.

7. To determine the electron number density as a function of time in a plasma afterglow, and to deduce the recombination rate from this measurement.

8. To develop a four pin probe for measuring the time resolved plasma
    electrical conductivity as a diagnostic for determining the elec-
    tron concentration.

9. To develop a method employing an equilibrium plasma for calibrating
    the electron conductivity probe.

10. To examine the possible use of optical diagnostic methods such as
    measurement of the emission of free-bound continuum radiation, as a
    means for obtaining a check on the data via an independent, redun-
    dant proceedure.

11. To assess the possible roles of the presence of the dimer ions Cs_2^+
    and ion clusters such as N_2Cs^+ and H_2OCs^+ (the water vapor will be
    present in small quantities as an impurity) in contributing to the
    measured recombination rates.

Status of Research

Research during the period February 1984 through January 1985 pro-
gressed from the numerical analysis of a proposed steady-state super-
sonic nozzle expansion experiment employing a high temperature plasma,
to conception and adoption of an alternative transient photoionization
afterglow experiment. During this period the analysis of the afterglow
experiment underwent extensive development and much of the necessary
hardware was specified and procured. This status report presents the
rational motivation, fundamental concepts, and major hardware designs
which were produced in the last contract year. Included herein are the
analyses by which the limitations of the nozzle expansion experiment and
the advantages of the pulsed experiment were determined. The afterglow
experiment and its essential hardware are described in detail.

In the Annual Report of March 1984 an experiment was suggested in
which an arc jet would be used to produce a plasma consisting of N_2 (or
some other molecular species) and thermally ionized Cs and then a rapid
expansion using a supersonic nozzle would be employed to produce steady-

state recombining conditions. Measurements of the electron number density, n_e, before and after the expansion would be compared with calculated values obtained from the electron continuity equation. Since the calculated values of n_e depend on the recombination coefficient $\alpha_{N_2}(T)$, such an experiment would provide a means for inferring the recombination rate.

Two non-dimensional parameters fundamental to any recombination experiment were identified in the last Annual Report. One parameter was the ratio of rates of recombination on molecules to recombination on electrons, $r = \alpha_{N_2} n_{N_2}/(\alpha_e n_e)$. In order that the recombination be dominated by the molecular third body process, it is desirable to have $r > 10$. The other parameter was the ratio of the characteristic time for recombination on N_2 to the residence time of a differential volume element of plasma, $\tau = (\alpha_{N_2} n_{N_2} n_e t_{res})^{-1}$. Since the equilibrium and frozen limits correspond to $\tau \ll 1$ and $\tau \gg 1$ respectively, a desirable value for τ would be $\tau \cong 1$.

Shown in Figures 1.1 and 1.2 are the results of numerical calculations for the variations of electron number density through a Mach 2 converging-diverging nozzle for various representative values of the upstream stagnation conditions that may be achievable with the steady-state gas flow system presently available in the High Temperature Gasdynamics Laboratory. The operating characteristics of the arc jet heater in that system limit the N_2 partial pressure to about four atmospheres, or in equivalent terms $n_{N_2} < 10^{25}$ m^{-3} for a plenum temperature of 3000 °K. (Figures 1b and 2b are for conditions which are somewhat more extreme.) The term "N_2 effect" refers to the value at the nozzle exit of the fractional decrease in n_e attributable to 3-body recombination with N_2, that is $[n_e(\alpha_{N_2}=0) - n_e]/n_e$. To obtain these results the Hinnov- Hirschberg expression [1.4] was used for $\alpha_e(T)$, and the theoretical expression proposed by Bates et al. [1.5] has been used for $\alpha_{N_2}(T)$. Sonic flow throughout a 10 cm long nozzle has been assumed in calculating residence time as $t_{res} = 0.005/\sqrt{T}$.

In the current grant period the necessity of determining $\alpha_{N_2}(T)$ in an experiment with only one molecular third body present and the
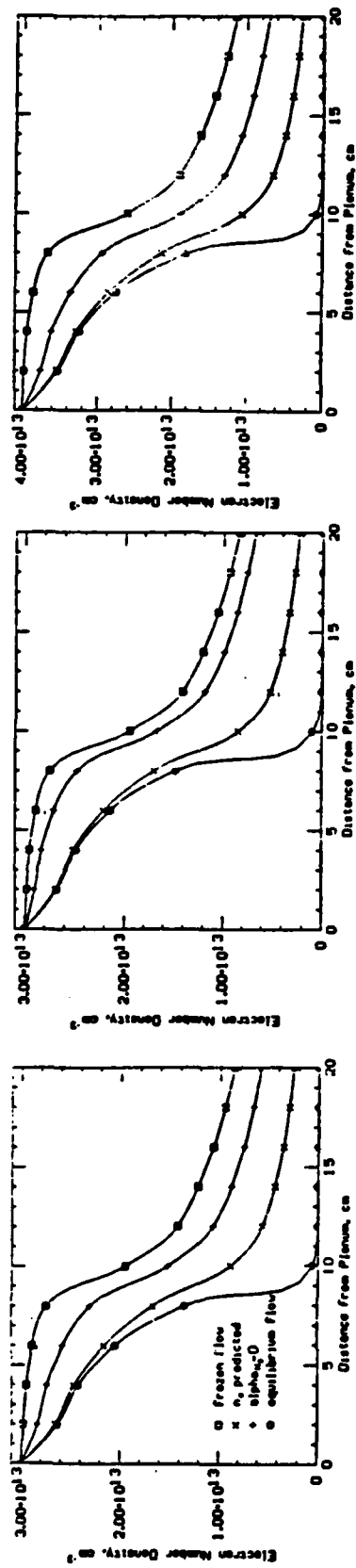
(a) $n_{H_2} = 10^{25} m^{-3}$, $n_e = 3 \times 10^{19} m^{-7}$

N_2 effect = 1.32

(b) $n_{H_2} = 2 \times 10^{25} m^{-3}$, $n_e = 3 \times 10^{19} m^{-3}$

N_2 effect = 1.86

(c) $n_{H_2} = 10^{25} m^{-3}$, $n_e = 4 \times 10^{19} m^{-3}$

N_2 effect = 1.57

Figure 1.1 Variation of electron density through the nozzle for a stagnation temperature of 2000°K.
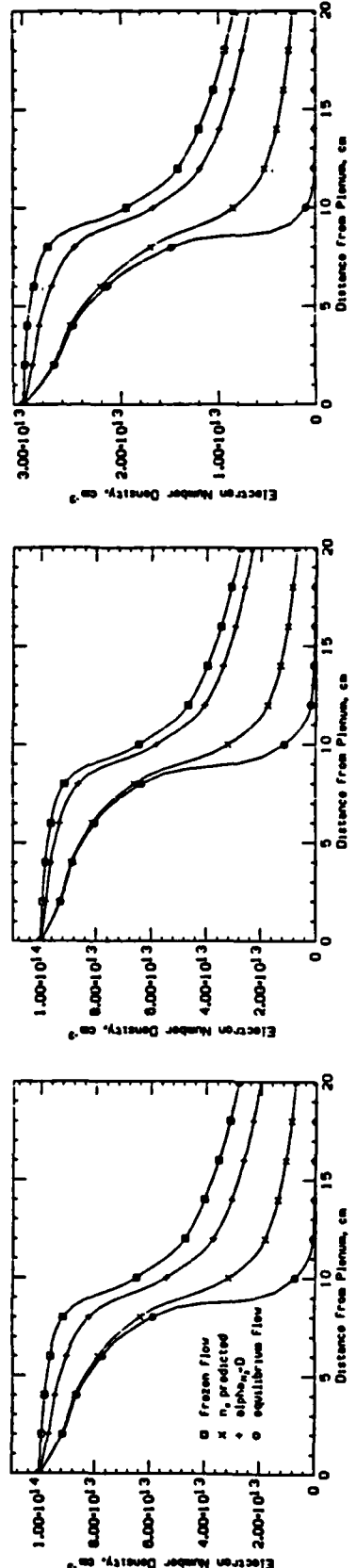
(a) $n_{N_2} = 10^{25} m^{-3}$, $n_e = 10^{20} m^{-3}$

N_2 effect = 1.70

(b) $n_{N_2} = 2 \times 10^{25} m^{-3}$, $n_e = 10^{20} m^{-3}$

N_2 effect = 2.26

(c) $n_{N_2} = 10^{25} m^{-3}$, $n_e = 4 \times 10^{-19} m^{-3}$

N_2 effect = 0.88

Figure 1.2 Variation of electron density through the nozzle for a stagnation temperature of 3000°K.

significance of the parameters r and τ has remained unchanged. The gasdynamic experiment has, however, been re-evaluated. In the following sections some limitations inherent to the steady-state expansion experiment are discussed. As an alternative approach, a pulsed experiment which creates an isothermal plasma via photoionization is shown to have many advantages.

Limitations of the Steady State Experiment

It appears from Figures 1.1 and 1.2 that in order for the value of n_e at the exit of the nozzle to depart significantly from the frozen value, it is necessary to have $τ < 1$, but this requirement then precludes achieving the condition $r > 10$. If n_e is decreased so as to increase r, the value of $τ$ is also increased, thereby reducing the effects of recombination relative to frozen flow. This behavior may be seen more clearly from the relation

$$\frac{r}{τ} = \frac{(n_{N_2} \alpha_{N_2})^2 t_{res}}{\alpha_e} \tag{1.5}$$

obtained by combining the expressions for r and $τ$ so as to eliminate n_e. For fixed N_2 partial pressure and nozzle dimensions, the right hand side of (1.5) is a function only of the stagnation temperature. Taking $P_{N_2} = 4$ atmospheres and $t_{res} = 0.005/\sqrt{T}$, one obtains $r/τ = 5.4$ for $T = 2000$ °K and $r/τ = 7.2$ for $T = 3000$ °K.

Another limitation of the rapid expansion experiment stems from the practical difficulties of providing optical access for diagnostic measurements of the expanding gas at more than a few axial locations (e.g. the plenum, the exit, and perhaps one intermediate position). Since the gas temperature decreases by approximately 1000 °K from the upstream plenum to the downstream exit, the accuracy of determining the temperature dependence of $\alpha_{N_2}(T)$ would be limited by the relatively coarse resolution with which the dependence on axial location of n_e could be measured.

- 9 -

Rather than following this path, an entirely different approach has been examined in which the required ionizational nonequilibrium is achieved by pulsed photoionization of Cs vapor instead of by a rapid expansion of a thermal plasma. This alternative approach appears to offer significant advantages.

Description of Pulsed Photoionization Experiment

The radiation source chosen for photoionization is a pulsed short arc Xe lamp directed along the axis of a tube containing the test gas (e.g. Cs vapor and N_2). A schematic of the arrangement is shown in Figure 1.3. The Cs vapor and N_2 are contained in a one inch diameter, twelve inch long inconel tube fitted with sapphire windows. The Cs pressure is one to ten torr and the nitrogen pressure is about one atmosphere. An electric tube oven heats the Cs-N_2 mixture in the temperature range 400 to 1200 K. The sapphire window has 75% transmission of radiation down to 200 nm wavelengths so it is transparent to photons capable of singly ionizing ground state Cs atoms, i.e. $\lambda <$ 318 nm, and opaque to photons capable of ionizing N_2, i.e. $\lambda <$ 200 nm. The Xe flash-lamp provides a 2 ms pulse of ionizing photons which is coupled to the Cs test cell through an ellipsoidal reflector.

A nonequilibrium, isothermal Cs plasma is produced by the radiation pulse. The free electrons are rapidly thermalized through collisions with the N_2. As the electrons begin to recombine with Cs^+ in the presence of the nitrogen, the electron number density would be determined as a function of time. Possible methods for obtaining the electron density include measurements of the spectral emission from free-bound and high lying bound-bound transitions in Cs, as well as measurements of the electrical conductivity using a four pin conductivity probe. The time history of the electron number density is directly related to the rate coefficient for recombination on N_2.

Experimental conditions would be chosen so that the recombination on N_2 proceeds at a much greater rate than electron loss by recombination on electrons, or by diffusion of electrons to the test cell walls. Under
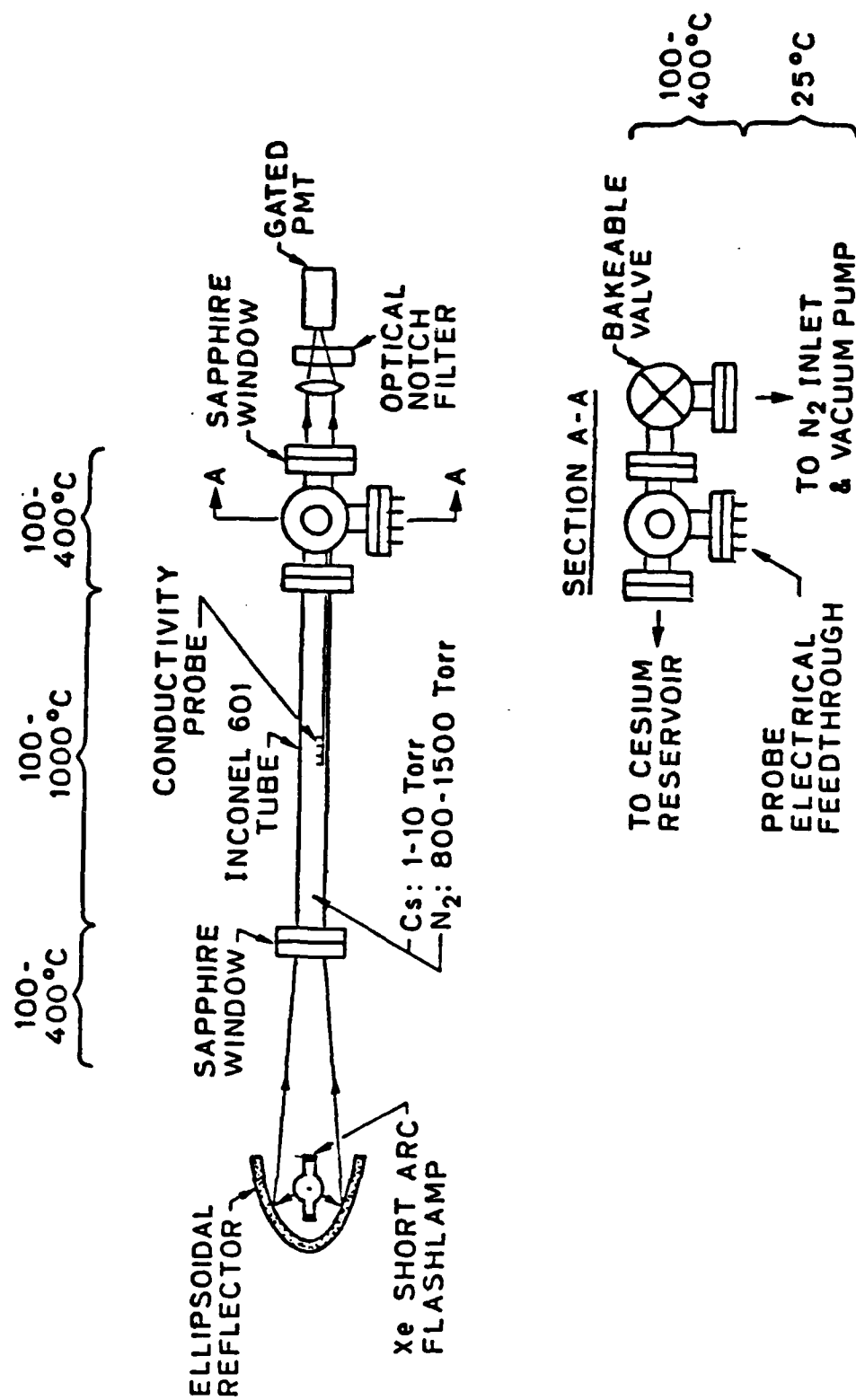
Figure 1.3 Pulsed photoionization experiment.

- 11 -

such conditions the electron kinetics are simply described by the differential equation

$$\frac{dn_e}{dt} = -\alpha_{N_2} n_{N_2} n_e^2 \, , \qquad (1.6)$$

which has the solution

$$\frac{1}{n_e} = \alpha_{N_2} n_{N_2} t + \frac{1}{n_{e_o}} \, . \qquad (1.7)$$

It is seen that the slope of the plot of $1/n_e$ vs time gives $\alpha_{N_2}(T)$ multiplied by the known concentration of N_2. The temperature dependence of $\alpha_{N_2}(T)$ is empirically determined by performing the experiment over the range of temperatures that can be achieved with the apparatus previously described.

The electron number densities corresponding to the parameter value $r = 10$ are given in Table 1.1. Also shown in the table are characteristic times for recombination on N_2, $t_{N_2} \sim (\alpha_{N_2} n_{N_2} n_e)^{-1}$, for electron diffusion to the walls, $t_{diff} \sim R^2/D_a \simeq KR^2 n_{N_2}/\sqrt{T}$, for the ionizing light pulse to decay from a peak to a minimum intensity, t_{pls}, and for thermalization of free electrons $t_{rlx} = [\nu_{e,N_2} \cdot 10 \cdot (2m_e/m_{N_2})]^{-1}$. Here $R \simeq$ 1 cm is the radius of the test cell, D_a is the ambipolar diffusion coefficient, K is a constant that depends on atomic properties of Cs+ and N_2 [1.6], ν_{e,N_2} is the average e,N_2 collison frequency [1.7], and $10 \cdot (2m_e/m_{N_2})$ is the average fraction of electron kinetic energy lost in all collisions with N_2 [1.8]. A typical value for the flashlamp pulse forming network is used for t_{pls}.

Table 1.1 shows that the characteristic times are ordered as $\tau_{rlx} \ll \tau_{pls} < \tau_{N_2} \ll \tau_{diff}$, and therefore that the experimental conditions result in an isothermal plasma dominated by recombination on N_2. The degree of excitation of N_2 by encounters with photons or energetic electrons is negligible. The N_2 molecules do not significantly absorb photons with wavelengths greater than 200 nm [1.9]. The energy corresponding to an electron liberated from the Cs ground state by a 200 nm photon is 2.1 eV. To excite a ground state N_2 to its first vibrationally

excited state requires approximately 0.22 eV [1.10], or each electron can excite at most 10 N_2 molecules. An estimate of the maximum fraction of N_2 molecules which could be excited in this manner is therefore $10 \cdot n_e/n_{N_2} < 10^{-6}$.

TABLE 1.1

Characterization of Pulsed Experiment

Temp, °K	n_e, cm^{-3}	t_{N_2}, sec	t_{diff}, sec	t_{pls}, sec	t_{rlx}, sec
400	3 X 10^{10}	7 X 10^{-3}	0.9	1 X 10^{-4}	4 X 10^{-9}
600	7 X 10^{10}	8 X 10^{-3}	0.5	1 X 10^{-4}	4 X 10^{-9}
800	2 X 10^{11}	7 X 10^{-3}	0.3	1 X 10^{-4}	4 X 10^{-9}

Advantages of the Pulsed Experiment

In essence, what is needed to determine $\alpha_{N_2}(T)$ is a measurement of the recombination rate in a plasma which is out of ionizational equilibrium and which contains only a single molecular species that can act as a third body for recombination. The pulsed photoionization experiment satisfies these requirements while avoiding many of the technical difficulties inherent in the steady-state, rapid expansion experiment. Since the plasma is stationary in the pulsed experiment, diffusion (not convection) determines the residence time of a plasma differential volume element. (Assuming diffusion is the major cause of electron loss behind three body recombination with N_2 implies that other loss mechanisms can be made insignificant. Loss mechanisms including electron attatchment and cluster formation like N_2Cs^+, which can be a precursor to dissociative recombination of Cs_2^+, are currently being evaluated. It is believed that conditions can be chosen so as to minimize the effects of all electron loss mechanisms as compared with diffusion and three body recombination on N_2.)

The characteristic time for the ambipolar diffusion of a Cs plasma in the one inch diameter cell containing N_2 at a pressure of one atmo-

⌣puᴇre is about 500 milliseconds, at 600 °K, or 4000 times longer than the convection-limited residence time in a 10 cm long sonic nozzle at 2000 °K. If the previously derived formula for r/τ is used with t_{res} replaced by t_{diff}, one obtains $r/\tau = 700$ at $T = 400$ °K and $r/\tau = 250$ at $T = 800$ °K. For the photoionization experiment, it is necessary to have $\tau \ [=(\alpha_{N_2} n_{N_2} n_e)^{-1}/t_{diff}] \ll 1$ (in contrast to the condition $\tau \approx 1$ for the rapid expansion experiment). It is possible to have this condition on τ satisfied and at the same time have $r > 10$ in the pulsed experiment.

The photoionization experiment creates an isothermal plasma because the kinetic energy of free electrons after photoionization is quickly thermalized. Recombination occurs at a constant temperature, and the temperature dependence of $\alpha_{N_2}(T)$ is measured directly by simply repeating the experiment at different temperatures. The large r/τ ratio obtainable in the pulsed experiment allows both r and τ to be chosen to simultaneously eliminate ambiguity about the role of the competing recombination on electrons and about the role of diffusion. In these respects the pulsed photoionization experiment appears to be more favorable than the steady-state rapid expansion experiment.

The Cesium Cell

Inconel 601 (Huntington Alloys) was chosen as the Cs tube wall material because of its exceptional ability to resist oxidation and spalling at temperatures up to 1530 K. The 1 inch diameter tube will be heated at atmospheric pressure in a tube oven to temperatures in the range between 400 and 1300 K, and it must withstand oxidation by air externally, and reduction by Cs internally. Where the inconel tube extends beyond the oven, the temperature will be maintained at 700 K by two independent ovens. This end temperature is the maximum working temperature of the sapphire windows (necessay for ionizing and diagnostic radiation), instrumentation feed-through (for the conductivity probe), and vacuum flanges. Because this hardware can not sustain the entire temperature range of the experiment, the cesium cell has end regions held at a different temperature than the center region.

The Cs vapor pressure will be controlled by carefully monitoring the temperature of the Cs reservoir. The reservoir will be maintained 20 to 50 K cooler than any other part of the system to prevent Cs condensation in other parts of the system. The oxygen-free copper reservoir and the N_2 supply and vacuum pump will be attached to the Cs cell by heated stainless steel tubing. The diffusion of the Cs vapor from the reservoir through the one inch diameter by 12 inch long tube to 90% of final concentration will occur in the time $t=0.47 \, x^2/D$ [1.11]. Here x is the tube length and $D = 0.0911 \, (T/288)^{3/2}$ cm^2/sec is the N_2-Cs binary diffusion coefficient. For T=400 K, t=1.85 hours. Although not unacceptably long, this mixing time will be decreased by natural convection.

The N_2 number density will be determined from simultaneous temperature and pressure measurements before the cell is heated. To not exceed the 1% uncertainty estimated for the thermocouple measurement, a 1% limit on pressure measurement uncertainty is set. This accuracy must hold over the pressure range 200 to 1500 torr (resulting from a final pressure of 1500 torr with final temperatures ranging from 400 to 1300 K.) These requirements will be met by a series of Wallace and Tiernan gages which span the desired pressure range.

The tube and reservoir will be attached via a bakeable valve to a liquid nitrogen trapped diffusion pump. Pressures of 10^{-8} torr will be achievable with this system in order to remove impurities during initial bake out and subsequent gas changes.

Photoionization

Photoionization of the Cs by Xe flashlamp radiation occurs through both one and two photon processes. The single photon process converts a ground state 6s electron to a free electron as represented by the reaction

$$Cs(6^2S_{1/2}) + h\nu_1 \rightarrow Cs^+ + e \qquad (1.8)$$
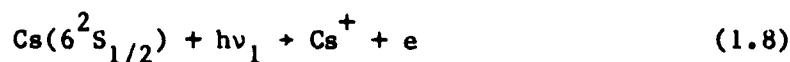
Here the photon energy, $h\nu_1$, must exceed the ionization potential of Cs, i.e. $\lambda < 318$ nm. Two-photon ionization first excites a ground state electron with a resonant photon; a second photon then ionizes the excited atom. The two steps are

$$Cs(6^2S_{1/2}) + h\nu_2 \rightarrow Cs^*(6^2P_{3/2,1/2}) \qquad (1.9)$$

$$Cs^*(6^2P_{3/2,1/2}) + h\nu_3 \rightarrow Cs^+ + e \qquad (1.10)$$
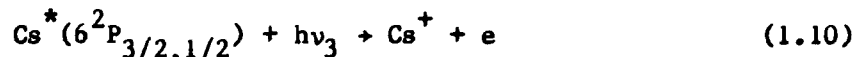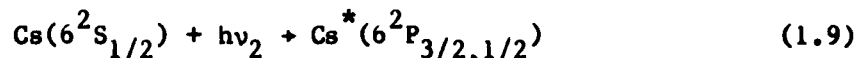
The resonance wavelengths are $\lambda_2 = 852$ nm (J=3/2) or $\lambda_2 = 894$ nm (J=1/2), and ionization from the 6p state can occur with any photon of wavelength shorter than $\lambda_3 < 508$ nm (J=3/2) or $\lambda_3 < 494$ nm (J=1/2). The cross sections for ionization from the 6s and 6p levels are approximately 10^{-19} cm^2 and 10^{-17} cm^2 respectively. Contributions from the two photon process to total free electron production are estimated to be substantial [1.12].

The experimental arrangement is greatly simplified by positioning the light source away from the Cs and the heat of the reaction zone. Placing the source outside the cell necessitates directing the light through a sapphire window at the end of the inconel tube. To produce a collimated, intense photon flux, a high radiance lamp is required. We have chosen a five atmosphere Xenon short arc lamp, (L-2369, manufactured by ILC Technology of Sunnyvale, CA.) This lamp has a seven mm arc length and a synthetic fused silica envelope. It is designed for pulsed operation at a maximum energy input of 300 Joules per pulse. Pulsed operation [1.13, 1.14] and the synthetic fused silica envelope enhance ultraviolet output from the lamp. The short arc lamp will be aligned along the axis of an ellipsoidal, aluminum reflector. (The A-5000, 1000 watt reflector is sold by Photon Technology inc., Princeton, N.J.). The arc is imaged at the far focus with f/2.5 optics by positioning the arc at the near focus of the ellipsoid. The resulting beam diverges with a half angle of 11 degrees, and it can be aimed directly through the sapphire window into the tube. Shallow incidence and high reflectivity of the polished metal tube interior surface will insure a uniform photon flux through the cell's length.

A multiple mesh pulse forming network has been designed to provide a roughly rectangular current pulse to the arc lamp. Pulse width will be 3 ms, and pulse height will be 1,700 amps. Begining from zero, the electron number density increases toward a value at which the rate of creation of electrons by photoionization equals the loss rate due to recombination. The equilibriuum electron density is approached asymptotically and the photon flux and pulse width must be great enough to produce sufficient ionization before the flash terminates. To have negligible interference by photoionization during the measured plasma decay, the current pulse will fall from its maximum value to zero in 0.9 ms. (Recombination will occur on the time scale of 7 ms ,see t_{N_2}, Table 1.1)

Diagnostics

A four pin plasma conductivity probe, developed at Stanford in connection with research on MHD plasmas, appears to be well suited for the work proposed here. The principle of operation of the probe is to measure the current I that flows when an ac voltage is applied between the outer pair of pins (i.e. electrodes) of a linear array of four pins, and to measure simultaneously the resulting potential difference δV between the inner pair of pins. Since J (current density) is proportional to I and δV is proportional to E (electric field), it follows from Ohm's Law, $E = J/\sigma$, that $\delta V = K\ I/\sigma$ and therefore that $\sigma = K\ dI/d(\delta V)$. Here σ denotes the electrical conductivity and K is a calibration constant that depends only on the geometric features of the probe. (In practice, $\delta V = K\ I/\sigma$ + constant, but this constant plays no role upon differentiation.) The constant K can be determined by immersing the probe in a liquid electrolyte (e.g. aqueous KCl) solution.

The conductivity is then related to the electron number density by the relation $\sigma = (n_e e^2)/(m_e \nu_{eh})$, where ν_{eh} is the electron-heavy collision frequency and e is the electronic charge. Temporal resolution of 50µs, corresponding to operation at 20 kHz has been demonstrated [1.15]. Initially this probe will be tested on a steady state thermal plasma. An equilibrium electron concentration of 3.6×10^{10} cm^{-3} can be

achieved by heating the Cs cell to 1300 K and the Cs reservoir to 630 K corresponding to a vapor pressure of 5 torr. The four pin probe measurement will be compared to equilibrium calculations of electron concentration based on Cs reservoir and cell temperature measurements. The probe will also be compared to optical diagnostic measurements.

Measurements of the recombination radiation continuum have been used to measure electron densities as low as 3×10^{13} cm^{-3} in the afterglow of a Cs-Ar discharge [1.16, 1.17]. In this work [1.16, 1.17] a monochromator was used for spectral filtering. By employing a 50 Å filter in place of the monochromator, calculations indicate it should be possible to increase the collected radiation by a factor of the order of 10^3 and therefore to lower the limit of measureable, transient n_e to about 10^{12} cm^{-3}. This limit can be lowered still further to 10^{10} cm^{-3} when measurements are made on a steady state plasma. Hence optical emission diagnostics should provide a check for the conductivity probe during testing on the thermal plasma. Upon successfull testing in a steady state plasma, the conductivity probe will be used to measure electron densities in the plasma afterglow.

At present, a simulated probe and high impedance amplifier have been built and tested with a 1 MΩ simulated plasma resistance. Successful performance has been obtained at frequencies up to 500 Hz. Higher frequency operation is hampered by capacitive coupling between probe leads. The problem of stray capacitance is currently being considered.

Summary

Because of the limitations of the nozzle experiment, effort was directed toward analyzing alternative experimental arrangements for producing the required nonequilibrium conditions. Among the alternatives considered, the approach that appeared most attractive was one in which the ionizational nonequilibrium would be achieved by pulsed photoionization of Cs vapor confined with N_2 in a heated test cell. The recombination coefficient $\alpha_{N_2}(T)$ would be determined by measuring the decay of n_e as a function of time, following the completion of the photoionization

pulse. In a photoionization experiment the recombination is non-steady in time and uniform in space, in contrast to a rapid expansion experiment which is steady in time and nonuniform in space.

Extensive calculations have been performed that demonstrate the feasibility of the photoionization approach. Possible diagnostic methods for measuring n_e in the range of plasma conditions expected have been reviewed, and a method based on measurement of the electrical conductivity (previously used in this laboratory in another context) appears feasible. The necessary high temprature materials plus vacuum and optical components have been designed and procured and some diagnostic development has been completed.

2.2 Discharge Effects: Plasma-Electrode Interaction

Introduction

The operating characteristics of practical plasma devices such as MHD generators, MPD thrusters, etc, are strongly affected by several limiting mechanisms associated with current transfer between electrodes and the plasma. Particular attention should be drawn to the excessive voltage drop and power dissipation in the plasma-electrode boundary layer, and the electrode erosion associated with both anodes and cathodes.

In spite of intensive research over many decades, the plasma- electrode boundary layer is still poorly understood [2.1,2.2]. The difficulty in analyzing this region stems from the complexities introduced by the interaction of electrical, thermal, fluid dynamic and electrode surface effects.

This work is directed towards providing a more complete understanding of the plasma-electrode interaction for the case of flowing, seeded, thermal plasmas at pressures of the order of one atmosphere, and involves both theoretical and experimental components.

Consider a channel flow of thermal plasma which might be either a noble gas or combustion products gas seeded to a suitable level (~ 1%) with cesium or potassium. We may define the electric boundary layer as that region near the channel walls, composed of high temperature insulators and electrodes, where charged particle nonequilibrium effects become significant and even dominant. Normally, the walls have to be operated at temperatures less than that of the core flow plasma because of material limitations.

On physical and dimensional grounds the region between the core plasma and the electrode surface can be divided into a number of overlapping layers of decreasing scale. Proceeding from the core plasma to the electrode these layers may be listed as follows (see Fig. 2.1):
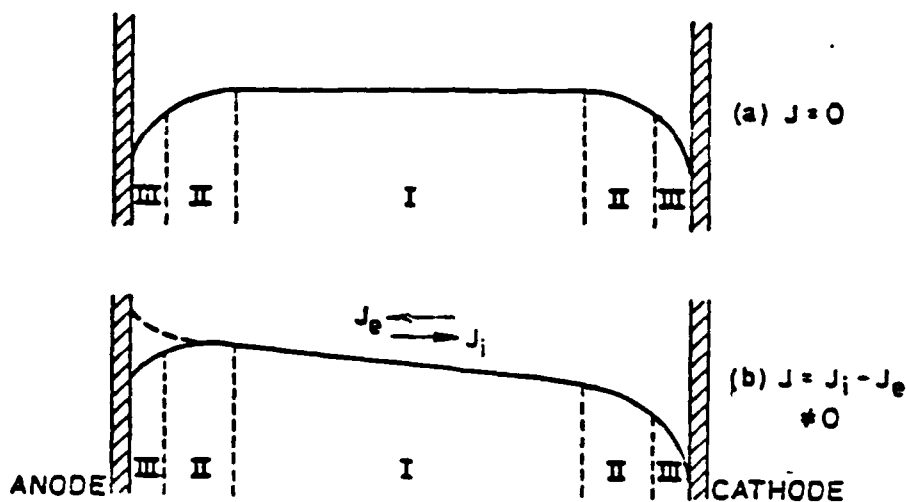
Figure 2.1.   Potential distribution across plasma diode.
I   Equilibrium Plasma
II   Ionization Non-Equilibrium Layer
III   Sheath. (Not to scale)

(i)   The gasdynamic boundary layer of scale $\delta \sim 10^{-2}$m, depending on distance along the channel, and comprising both a velocity and thermal boundary layer.

(ii)   The ionization nonequilibrium (or ambipolar diffusion) layer of scale ℓ_R, the characteristic ion recombination length.

(iii)   The sheath of scale equal to the Debye length $\lambda_D \equiv (\epsilon_o kT/n_\infty e^2)^{1/2}$, typically 10^{-6}m. In this layer charge neutrality is not preserved and large electric fields develop.

(iv)   The Knudsen layer where free molecule flow takes over from a continuum (fluid) description and the appropriate scale is the mean free path. The mean free paths for electrons and ions are of order $\ell_e \sim \ell_i \sim 10^{-6}$m and are thus comparable to λ_D.

It should be emphasized that the four layers distinguished above are overlapping and no sharp boundaries can be distinguished. Moreover, the scale lengths are nominal ones based on freestream rather than local conditions. In general the scale lengths are ordered according to $\delta \gg \ell_R \gg \lambda_D \sim \ell_e \sim \ell_i$.

As the current density J is increased from zero, the potential drop at the cathode increases and more ions than electrons are collected. The reverse happens at the anode. However, these conditions only hold for very small currents $J < J_i$, the random ion current ($\lesssim 10$ mA/cm^2). For higher currents, of technical interest, the cathode must emit electrons. Of the known emission processes, both secondary emission due to ion bombardment and thermionic (including field-assisted, Schottky emission) are relevant. Depending on conditions, particularly the cathode material, temperature and work function, diffuse emission persists up to some current density when there is a transition to a constricted discharge terminating in an arc cathode spot.

At the anode it might be expected that large currents up to $J \sim J_e$, the random electron current (~ 10 A/cm^2), could be collected as a result of the reducing sheath potential drop. However it is commonly observed that constrictions in the form of anode glow spots occur at lower currents and the sheath potential drop may change sign as indicated in Fig. 2.1. The reason for this behavior is unexplained, but it is probably related to the creation of a highly conducting discharge channel which penetrates the lower conductivity boundary layer plasma.

From the foregoing discussion it is clear that the physical processes involved are extremely complex and experimental data are vital to guide the theoretical modeling.

Research Objectives

1. To observe and record the current-voltage characteristics and the transition from diffuse to constricted discharge modes for electrodes immersed in a flowing, atmospheric pressure thermal plasma.

2. To predict the current-voltage characteristics for anodes and cathodes and to compare these predictions with the experimental results.

3. To use the insight provided from objectives 1 and 2 above to more fully understand the constriction process.

Status of Research

The present research is comprised of both theoretical and experimental components. To date, the theoretical aspects of the project have been stressed.

Theoretical Work

The approach adopted for theoretical modeling is to start off with the simplest relevant model and to introduce the complexities of the complete problem one at a time. To this end, the plasma-sheath problem for a plane electrode in contact with a <u>uniform</u>, equilibrium, weakly-ionized plasma has been formulated in some generality. By assuming that the plasma is isothermal and stationary, the complexities associated with the gasdynamic thermal boundary layer and Joule heating are, for the present, eliminated and the essential plasma physics aspects of the problem are clearly revealed.

This formulation in terms of the conservation equations for the electron and ion concentrations and momenta (including inertia), together with Poisson's equation, gives a uniform description of the ionization nonequilibrium layer and sheath, in both the collionless and collision dominated regimes, without having to resort to an arbitrary division and matching of the separate regions.

In the current reporting period this plasma-sheath problem has been investigated in the continuum (collision-dominanted) limit, neglecting the inertia terms. In this case, the governing equations are:

$$\frac{d\overline{\Gamma}_e}{d\overline{x}} = \overline{\dot{n}} = \left(1 - \overline{n}_e \, \overline{n}_i\right) \overline{n}_e \qquad (2.1)$$

$$\frac{d\overline{\Gamma}_i}{d\overline{x}} = \overline{\dot{n}} = \left(1 - \overline{n}_e \, \overline{n}_i\right) \overline{n}_e \qquad (2.2)$$

$$\frac{d\overline{n}_e}{d\overline{x}} = - \overline{n}_e \, \overline{E} - \frac{4\mu}{(1 + \mu)} \overline{\Gamma}_e \qquad (2.3)$$

$$\frac{d\overline{n}_i}{d\overline{x}} = \overline{n}_i \, \overline{E} - \frac{4}{(1 + \mu)} \overline{\Gamma}_i \qquad (2.4)$$

$$\frac{d\overline{E}}{d\overline{x}} = \frac{1}{\epsilon^2} \left(\overline{n}_i - \overline{n}_e\right) \qquad (2.5)$$

together with the subsidiary relations

$$\overline{J} = \frac{4\mu}{(1 + \mu)^2} \left(\overline{\Gamma}_i - \overline{\Gamma}_e\right) \qquad (2.6)$$

$$\overline{\phi} = - \int_0^x \overline{E} \, d\overline{x} \qquad (2.7)$$

Here x is normalized on the ion recombination distance $\ell_R \equiv (2D_a/\beta n_\infty^2)^{1/2}$ where D_a is the ambipolar diffusion coefficient and β is the three-body recombination coefficient. The electron and ion concentrations are normalized on n_∞ while the net generation rate $\dot{n}$ is normalized on $\beta \, n_\infty^3$. The potential ϕ is normalized on (kT/e) while the electric field is normalized on $E_R \equiv (kT/e\ell_R)$. The fluxes are normalized on $\Gamma_R \equiv (2D_a n_\infty/\ell_R)$ and the current density is normalized on $J_R \equiv e n_\infty (\mu_e + \mu_i) E_R \equiv \sigma_\infty E_R$ where σ_∞ is the electrical conductivity for $\overline{x} \to \infty$.

There are three parameters to be specified: the mobility ratio $\mu \equiv (\mu_i/\mu_e) \ll 1$, a function only of the type of ion and background gas; $\epsilon = (\lambda_D/\ell_R) \ll 1$, the ratio of the Debye length to the ion recombination length; and $\overline{J}$, the normalized current density.

- 24 -

In view of Eq. (2.6), four independent boundary conditions are required for solution of the five coupled, first order, nonlinear differential equations (2.1)-(2.5). In the continuum limit two of these are $\overline{n}_e = \overline{n}_i = 0$ at $\overline{x} = 0$. The other two, $\overline{E}$ and either $\overline{\Gamma}_e$ or $\overline{\Gamma}_i$, are chosen such that the solution goes over, at large $\overline{x}$, to the quasi-neutral solution derived earlier [2.3].

In this quasi-neutral solution we put $\overline{n}_e = \overline{n}_i = \overline{n}$ and discard Poisson's equation (2.5) to obtain the analytic results:

$$\overline{n} = \tanh \overline{x} \tag{2.8}$$

$$\dot{\overline{n}} = \operatorname{sech}^2 \overline{x} \tanh \overline{x} \tag{2.9}$$

$$\overline{\Gamma}_e = -\frac{1}{2} \operatorname{sech}^2 \overline{x} - \frac{(1 + \mu)}{4\mu} \overline{J} \tag{2.10}$$

$$\overline{\Gamma}_i = -\frac{1}{2} \operatorname{sech}^2 \overline{x} + \frac{(1 + \mu)}{4} \overline{J} \tag{2.11}$$

$$\overline{E} = \left[- \left(\frac{1 - \mu}{1 + \mu} \right) \operatorname{sech}^2 \overline{x} + \overline{J} \right] \coth \overline{x} \tag{2.12}$$

$$\overline{\phi} = \ln \tanh \overline{x} - \overline{J} \ln \sinh \overline{x} \tag{2.13}$$

It is noteworthy that $\overline{E}$ has a simple pole and $\overline{\phi}$ has a logarithmic pole at $\overline{x} = 0$. Moreover, for a cathode, for $\overline{J} < - 2\mu/(1 + \mu)$, $\overline{\Gamma}_e$ becomes positive and electron emission is implied. Furthermore, for an anode $\overline{E}$ changes sign (corresponding to a positive anode fall) for $\overline{J} > (1 - \mu)/(1 + \mu)$, and $\overline{\Gamma}_i$ becomes positive, indicating ion emission for $\overline{J} > 2/(1 + \mu)$.

The profiles of $\overline{n}$ and $\dot{\overline{n}}$ are shown in Fig. 2.2, while the potential profiles for various $\overline{J}$ are shown in Fig. 2.3.

Integration of the full plasma-sheath equations (2.1)-(2.5) has proven rather difficult. Initially a "shooting" technique was used, in which the initial values of $\overline{E}$ (0) and $\overline{\Gamma}_i(0)$ (or $\overline{\Gamma}_e(0)$) were adjusted by iteration to obtain the solution best matching the quasi-neutral
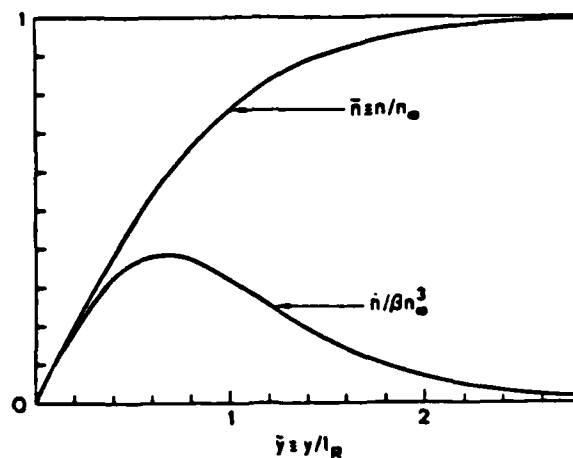
Figure 2.2. Profiles of normalized charged particle concentrations and net generation rate.
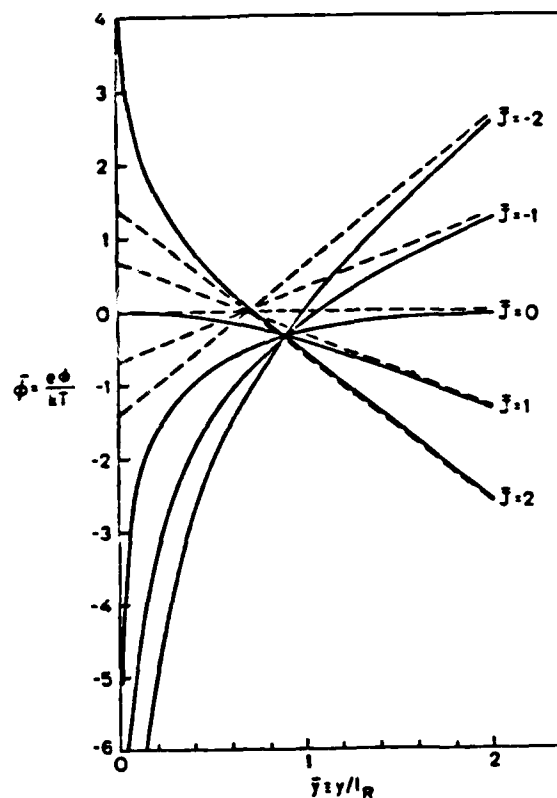

Figure 2.3. Profiles of the normalized potential as a function of normalized current density: $\bar{J} < 0$, cathode; $\bar{J} > 0$, anode. Broken lines indicate the asymptotes corresponding to the uniform electric field in the distance plasma.

solution (Eqs. 2.8-2.13) at large $\bar{x}$. It was found that the solution was extremely sensitive to the choice of $\bar{E}(0)$ and that it invariably became unstable for $\bar{x} > 2.5$.

Recently, the method of quasilinearization with orthonormalization has been utilized whereby, in addition to the boundary conditions $\bar{n}_e(0) = 0$, $\bar{n}_i(0) = 0$, the boundary conditions are imposed that $\bar{\Gamma}_e(\bar{x})$ and $\bar{E}(\bar{x})$ satisfy Eqs. (2.10) and (2.12) at some large $\bar{x}$, e.g. $\bar{x} = 4$.

Typical results for the case $\mu = (1/300)$, $\varepsilon = 10^{-1}$ and various values of J are shown in Figs. 2.4 through 2.7. In these solutions the quasi-neutral ionization nonequilibrium region merges smoothly into the sheath region where $n_i \neq n_e$. One can arbitrarily choose to take the plasma-sheath boundary at $\bar{x}_s$ where $|n_i - n_e|/(n_i + n_e) = \delta$, a small parameter. Referring to Fig. 2.4 for $J = 0$, it is seen that a reasonable choice is $\delta = 0.1$. This gives a sheath thickness of $\bar{x}_s = 0.82$ or $x_s = 8.2\lambda_D$, a potential fall across the sheath of $\bar{\phi}_s = 6.4$ and a potential fall through the ionization nonequilibrium layer of $\bar{\phi}_R = 1.1$. The criterion $\delta = 0.1$ is taken as corresponding to the plasma-sheath boundary in all the cases shown.

In Fig. 2.4 for $J = 0$, it is seen that $\bar{n}_i$ and $\bar{n}_e$ lie well below the quasi-neutral value $\bar{n} = \tanh \bar{x}$ out as far as $\bar{x} = 3$. As a result the region of net generation, $\dot{\bar{n}}$ moves to larger $\bar{x}$ than in the quasi-neutral solution. Also for this case $\bar{\Gamma}_e = \bar{\Gamma}_i$ everywhere, tending to zero at large $\bar{x}$ and to $-1/2$ at $\bar{x} = 0$. The net generation of electron ion pairs generates the equal fluxes which flow to the electrode.

Figures 2.5-2.6 show solutions for anodes $(J > 0)$ as the current is increased. For $J < 1$, the potential fall in the anode sheath is negative and there is an ion sheath. For $J = 1$, illustrated in Fig. 2.5, there is no sheath and $\bar{n}_e$ and $\bar{n}_i$ closely follow the quasi-neutral approximation $\bar{n} = \tanh \bar{x}$. For $J > 1$ the potential fall becomes positive and there is an electron sheath as is clear from Fig. 2.6 for $J = 2$. The sheath thickness and potential fall for this case are $\bar{x}_s = 0.47$, and $\bar{\phi}_s = -1.87$. As J increases the electron sheath thickens and the potential
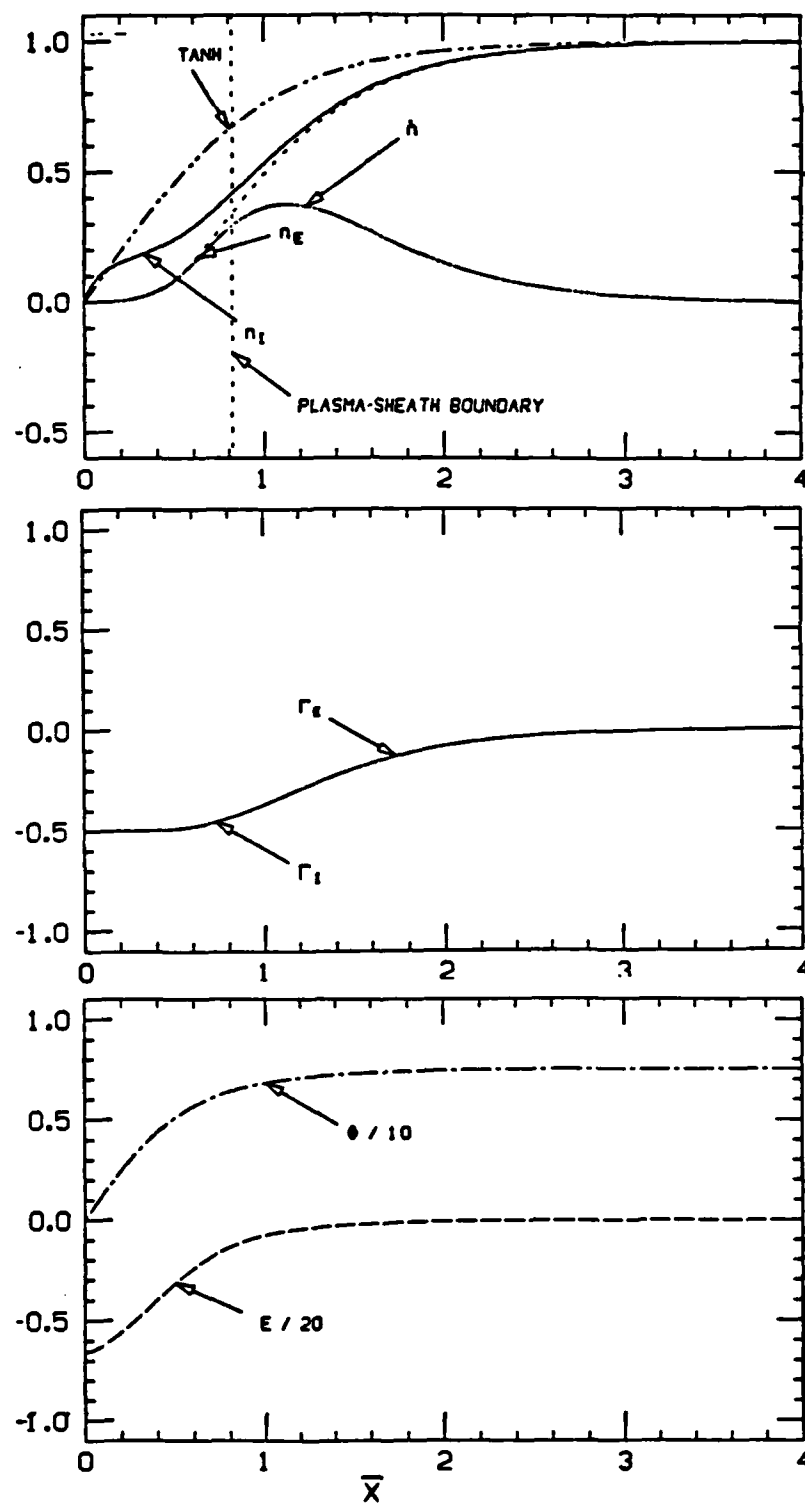
Figure 2.4.   Solution for $\mu = 1/300$, $\varepsilon = 10^{-1}$ and $J = 0$.
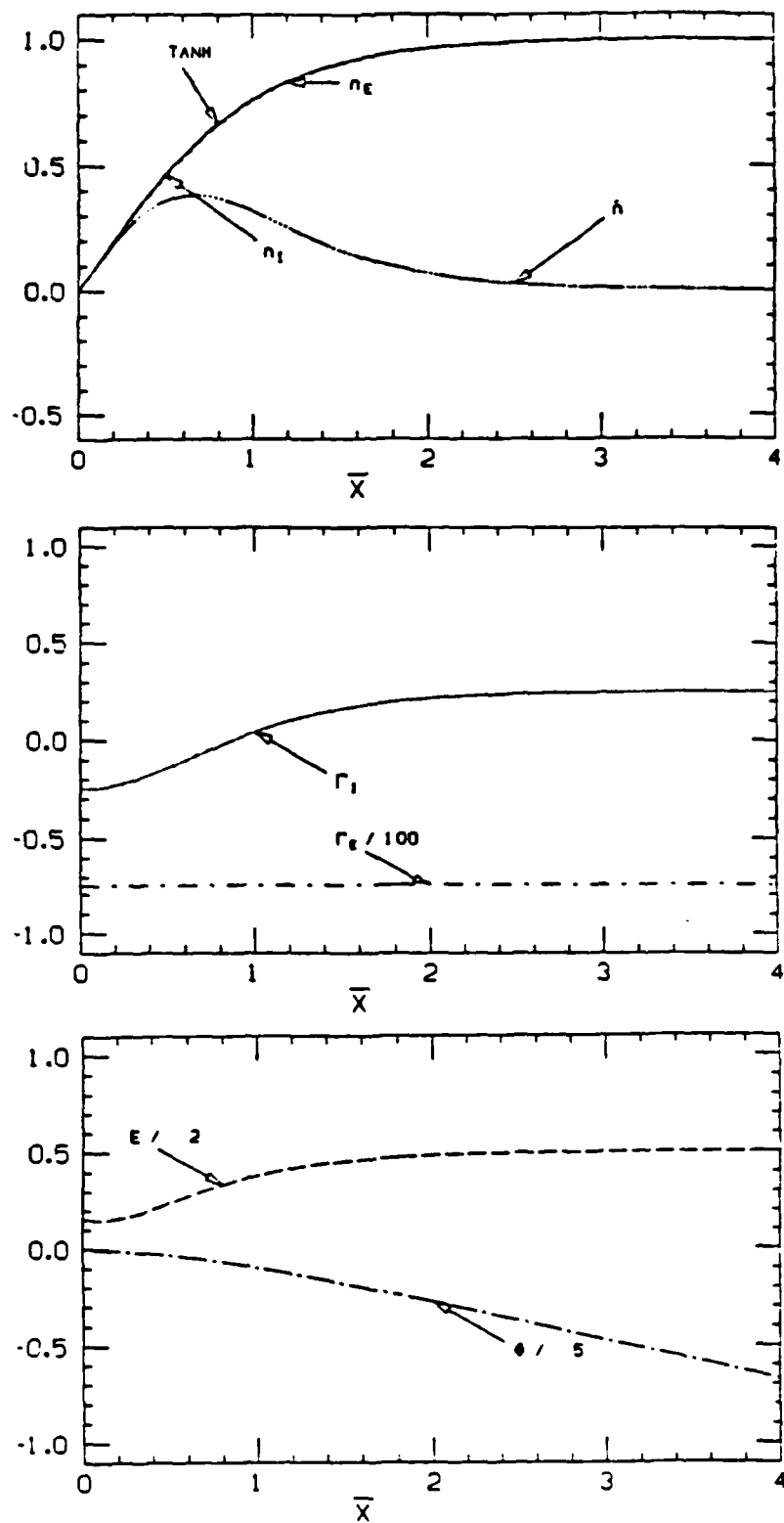
Figure 2.5. Solution for $\mu = 1/300$, $\epsilon = 10^{-1}$ and $J = 1$ (anode).
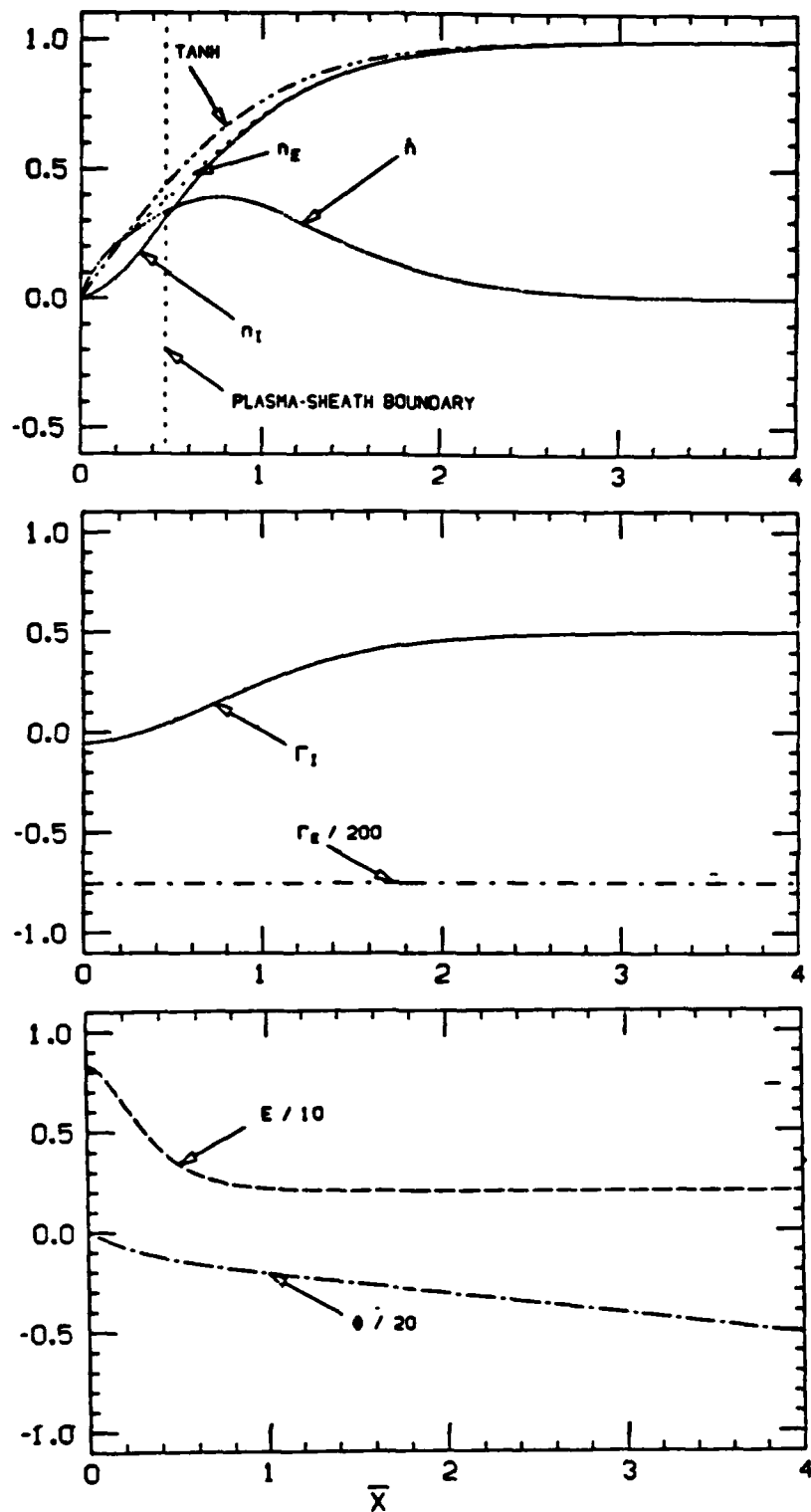
Figure 2.6. Solution for $\mu = 1/300$, $\epsilon = 10^{-1}$ and $J = 2$ (anode).

drop increases. These results are in accord with the results from the quasi-neutral approximation. All values of the potential fall through the sheath are given by the difference between the calculated potential and the potential due to the (assumed) uniform conductivity of the plasma.

Figure 2.7 shows the solution for a cathode with $J = -2\mu$. For this case the electron flux to the cathode is reduced to zero and for larger currents $\Gamma_e(0)$ becomes positive, indicating electron emission as predicted by the quasi-neutral approximation. For $J = -2\mu$, the current at the cathode is carried by arriving ions, while the net volume generation of electrons provides the current in the distant plasma, which is carried primarily by electrons. Compared with the case $J = 0$ (Fig. 2.4), the cathode with $J = -2\mu$ shows an increase of the ion sheath thickness from $\overline{x}_s = 0.82$ to 1.19 and an increase of sheath potential drop from $\overline{\phi}_s = 6.44$ to $\overline{\phi}_s = 12.71$. With larger currents the cathode sheath thickness and potential drop can be expected to increase significantly.

Numerical convergence was observed to be quite slow for anode cases with $J > 2$ and cathode cases with $J < -2\mu$. This has led to a re-examination of the applicability of the continuum boundary conditions, i.e., $\overline{n}_i(0) = \overline{n}_e(0) = 0$. It is worthy to note that the convergence significantly slowed for anode/cathode cases where ion/electron emission by the electrode was expected. Considering first the cathode cases; electron emission may be expected to create a non-zero value for $\overline{n}_e$ at the electrode surface. Indeed, by constraining only $\overline{n}_i(0) = 0$ and requiring that $\overline{n}_e(\overline{x})$ satisfy Eq. (2.8) at a large value of $\overline{x}$, the calculations predict that $\overline{n}_e(0) = 0.091$ for $J = -2\mu$. The resulting solution is shown in Fig. 2.8. This implies a very thin electron sheath immediately adjacent to the electrode surface followed by a thicker ion sheath. Comparison of Figs. 2.7 and 2.8 shows that the latter solution follows the quasi-neutral prediction much more closely. The sheath thickness and potential fall are found to be $\overline{x}_s = 0.32$ and $\phi_s = 1.13$ compared with the much larger values $\overline{x}_s = 1.19$ and $\phi_s = 12.71$ calculated previously. This is to be expected because now the ion sheath near the electrode has been partly neutralized by electrons.
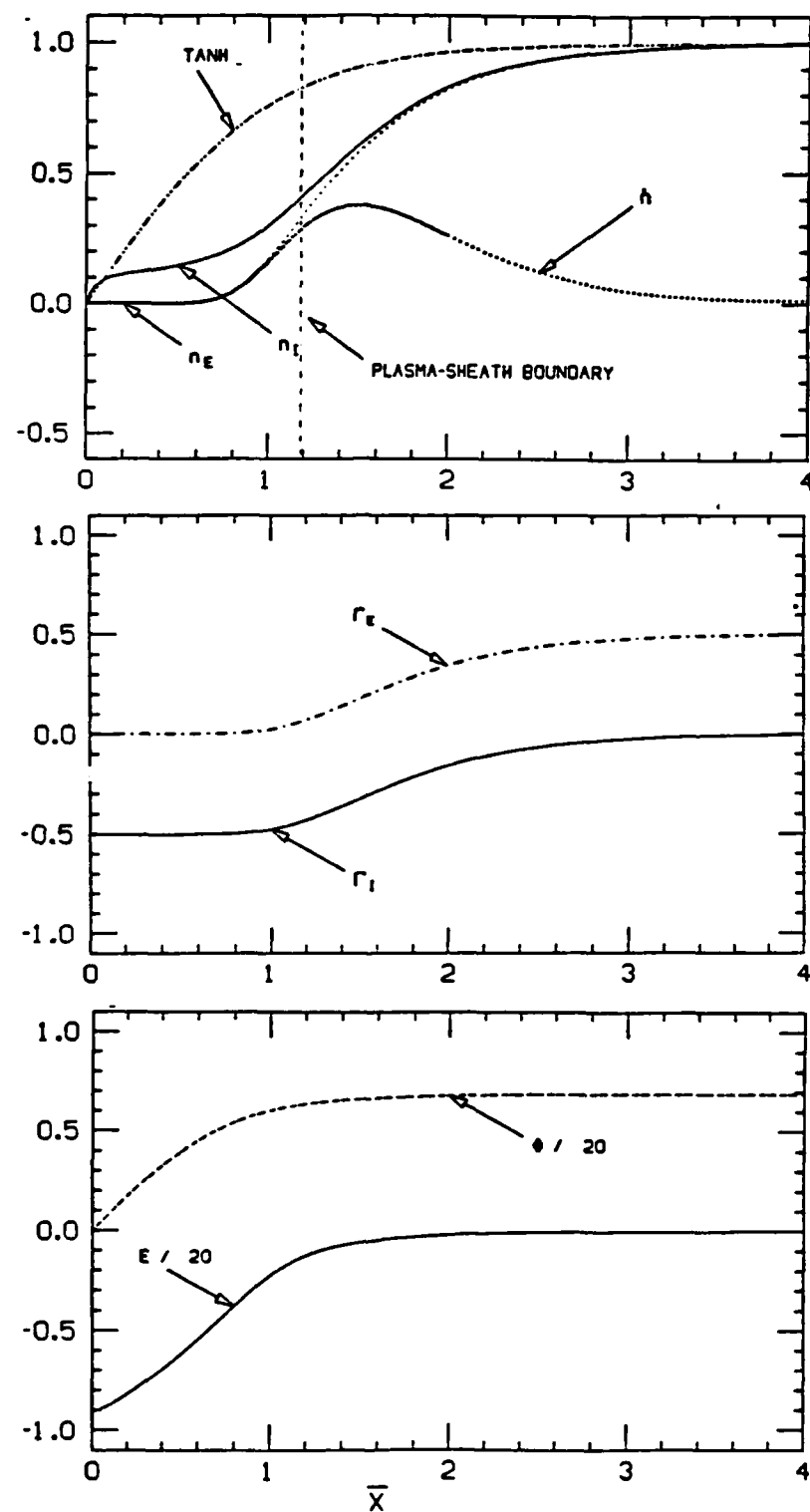
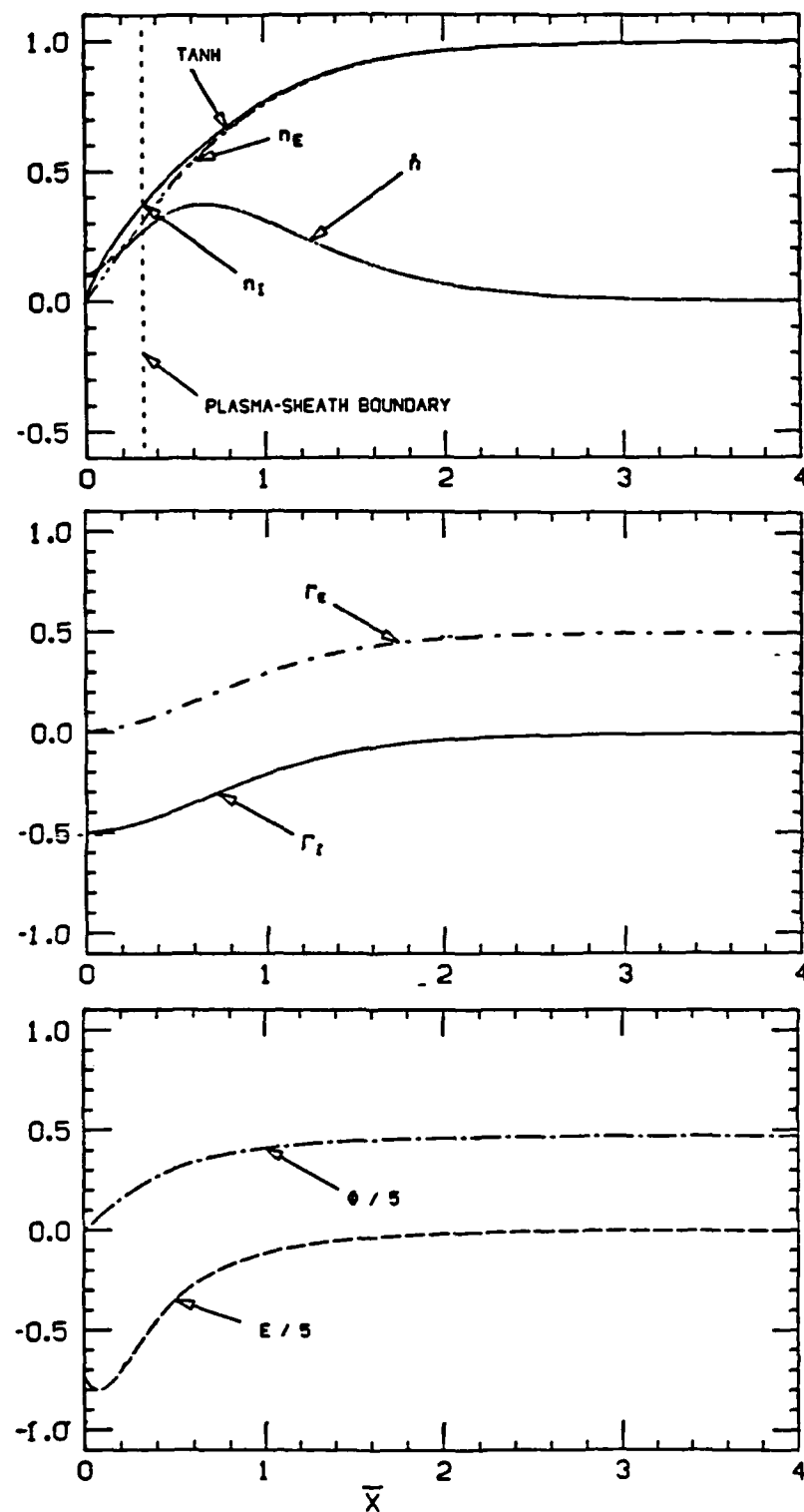Figure 2.7. Solution for $\mu = 1/300$, $\varepsilon = 10^{-1}$ and $J = -2\mu$.

Figure 2.8   Solution for $\mu = 1/300$, $\varepsilon = 10^{-1}$ and $\overline{J} = -2\mu$
with only $\overline{n}_i(0) = 0$.

It is clear that this system of equation is extremely sensitive to the electrode surface boundary conditions.

Application of the same boundary conditions for the $J = 0$ case leads to the solution shown in Fig. 2.9. Here we find that $\overline{x}_s = 0.31$ and $\overline{\phi}_s = 1.13$ compared with $\overline{x}_s = 0.62$ and $\overline{\phi}_s = 6.4$ found previously.

As the current increases we expect the sheath to disappear near $J = 1$. Using an argument similar to that above, we choose to constrain $\overline{n}_e(0) = 0$ and require $\overline{n}_i(\overline{x})$ to satisfy Eq. 2.8 at a large value of $\overline{x}$ for positive currents whereby we expect ion emission from the anode. We find for $\overline{J} = 2$ that $\overline{n}_i(0) = 0.071$, $\overline{x}_s = 0.29$, and $\overline{\phi}_s = 0.72$. This may be compared with $\overline{x}_s = 0.47$, and $\overline{\phi}_s = 1.87$ found before. This solution is plotted in Fig. 2.10.

The above results show the critical role that the boundary conditions play in the solution of this problem. The derivation of physically realistic boundary conditions when there is electron or ion emission from the electrode represents a major goal of this project.

Experimental Work

The experimental work is being conducted in a versatile 5 KW thermal diffusion flame burner capable of producing a combustion plasma to 3000K and seeded to 1% by mass of potassium vapor to provide a conductivity of up to 10 S/m. This facility was built in connection with an earlier NSF grant for the testing of plasma diagnostic techniques.

The burner is presently constructed with a water-cooled, ceramic-lined chimney. The chimney inside dimensions measure 2.5 cm by 8.75 cm. The test section consists of a small volume within the chimney assembly. Optical access is provided by two 2.5 cm diameter quartz windows. Gas temperature measurements throughout the test volume and ceramic surface temperature measurements have been made for a variety of flow conditions. Typical results for the center-line gas temperature and ceramic surface temperature are given in Figs. 2.11 and 2.12. These data are for a relatively cool methane/air flame with a fuel/air ratio of 1.2.
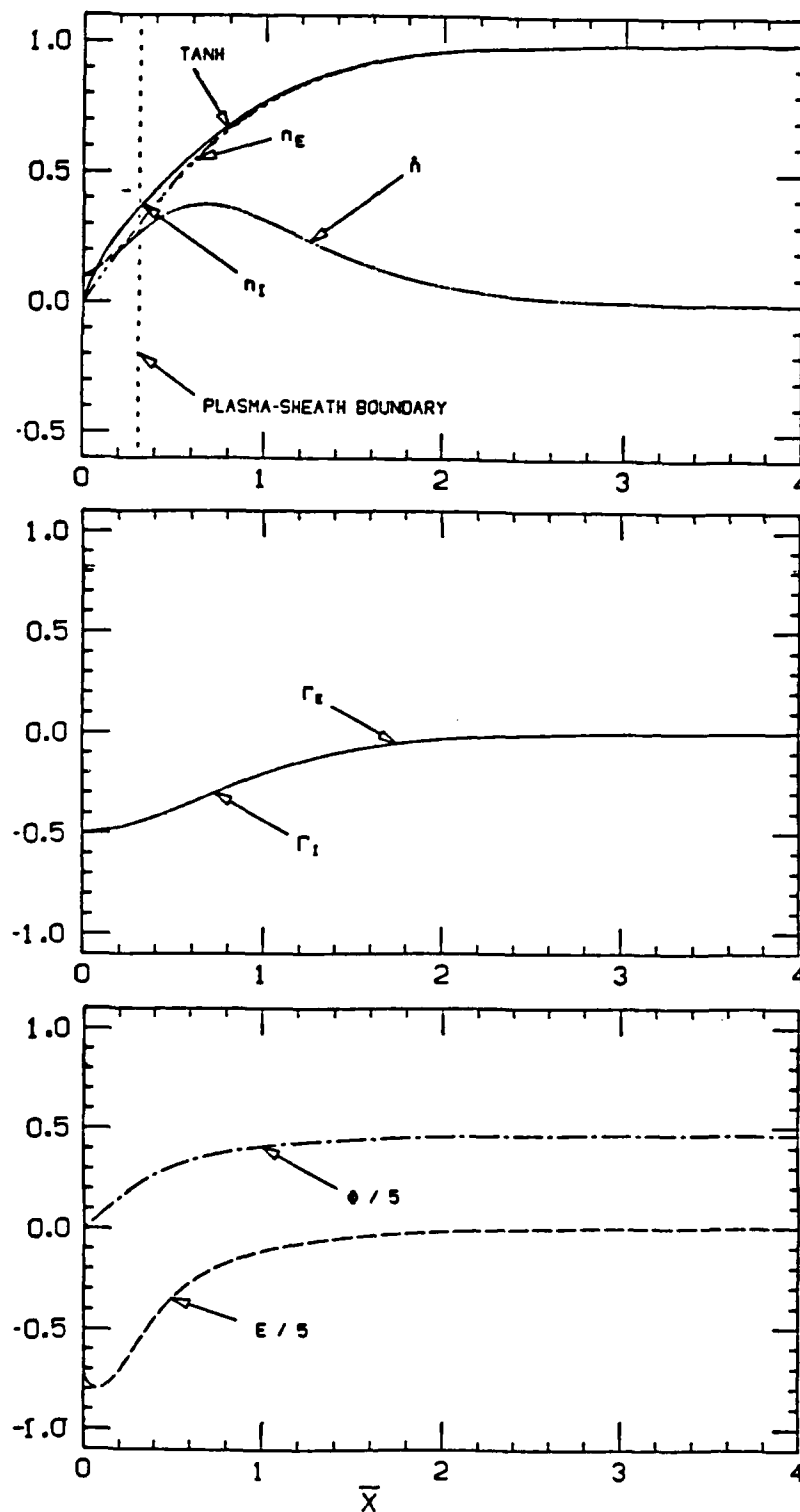
Figure 2.9. Solution for $\mu = 1/300$, $\varepsilon = 10^{-1}$ and $\bar{J} = 0$ with only $\bar{n}_i(0) = 0$.
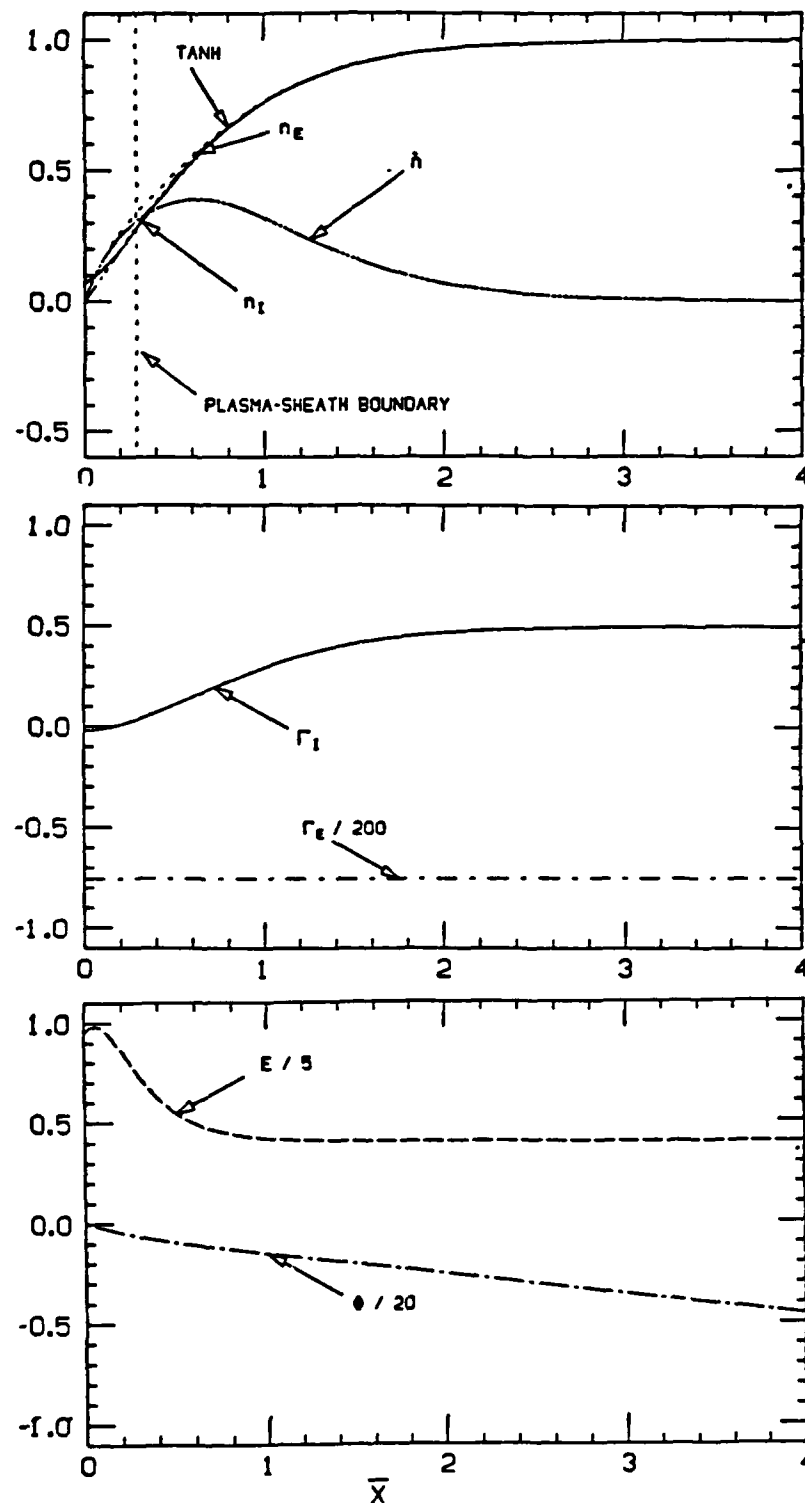
Figure 2.10. Solution for $\mu = 1/300$, $\varepsilon = 10^{-1}$ and $\overline{J} = 2$ with only $\overline{n}_e(0) = 0$.
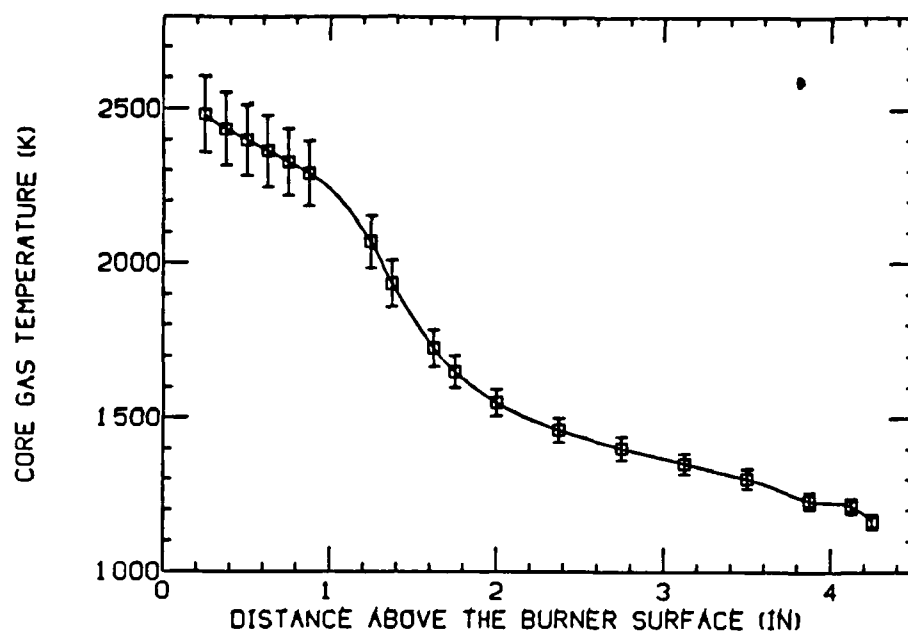
- 36 -

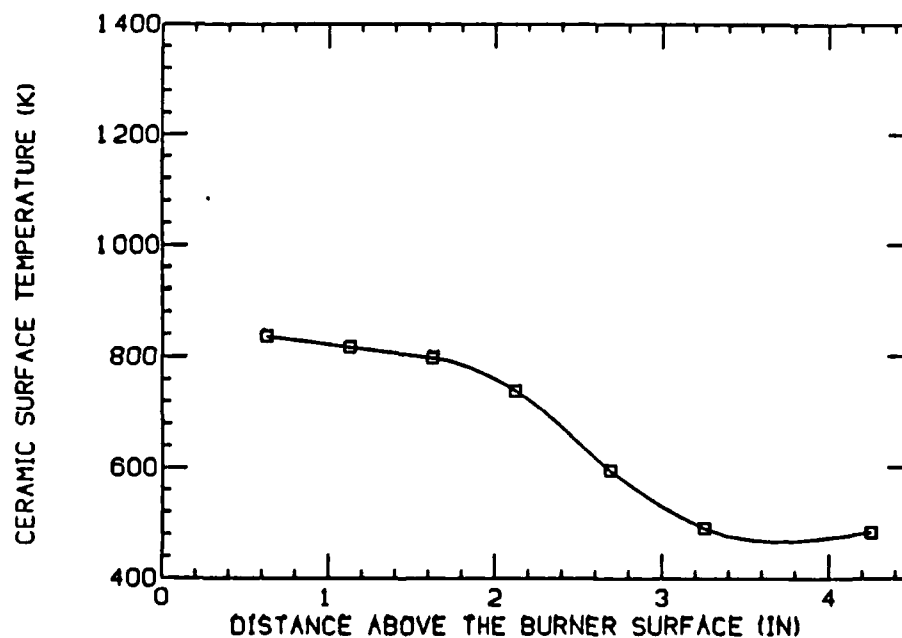Figure 2.11. Gas center-line temperatures for methane/air flame.

Figure 2.12 Ceramic surface temperatures for methane/air flame.

Electrode experiments will be conducted using more energetic reactants such as hydrogen/methane/oxygen mixtures to obtain higher temperatures and electrical conductivities. The center-line gas
temperature for a portion of the test volume (up to the melting point of the thermocouple) and the ceramic surface temperature for such a flame are plotted in Figs. 2.13 and 2.14. These data were taken for a fuel mixture with a hydrogen/carbon ratio of 12 and a fuel/air ratio of 1.2.

It is desirable to place the electrodes approximately 4 - 5 cm above the burner surface. Unfortunately, this region is presently marked by a steep axial gas temperature gradient. For this reason, an improved test section is being constructed with smaller optical ports and increased thermal insulation of the chimney, to achieve a more uniform axial temperature profile.
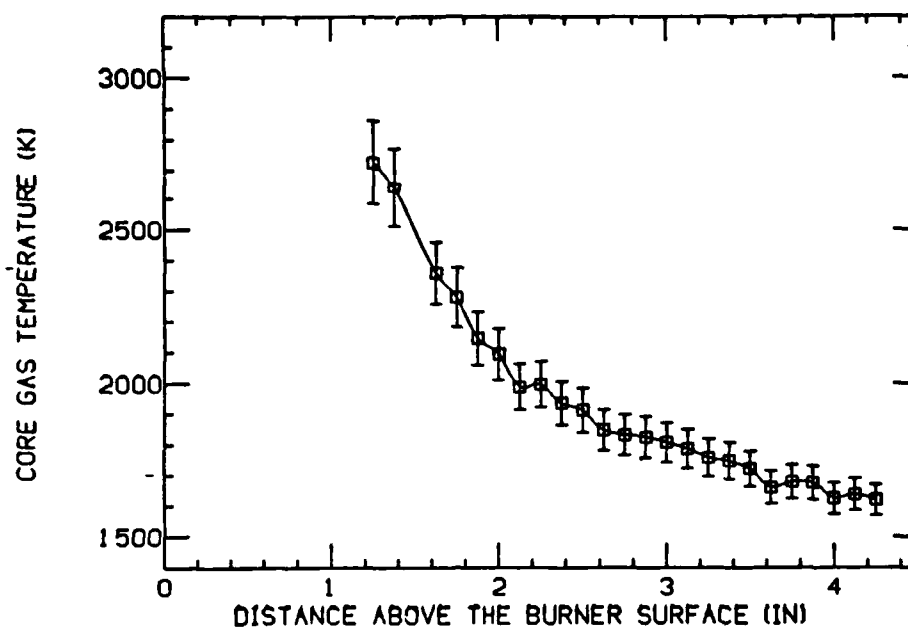
Figure 2.13. Gas center-line temperatures for
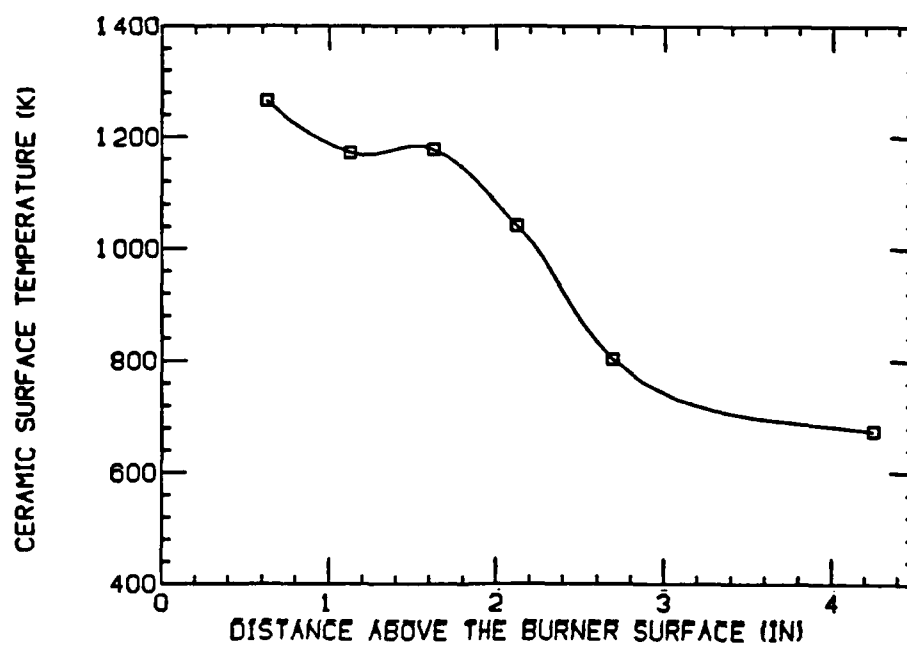hydrogen/methane/oxygen flame.

Figure 2.14. Ceramic surface temperatures within the test section
for hydrogen/methane/oxygen flame.

2.3 Interaction of Discharges and Fluid Dynamics

Introduction

In several space power and propulsion systems of potential interest to the Air Force, such as MPD thrusters and MHD generators, fluid motions induced by discharges are of critical importance to both the understanding and performance of the system. In any MHD device the electromagnetic field may affect the plasma flow field in several ways. Among these effects are the following:

(1) the effect of Joule heating on plasma temperatures;

(2) the Hartmann effect;

(3) turbulence suppression; and

(4) the generation of secondary flows.

The first three of these effects have been the subjects of previous studies performed at HTGL [3.1-3.4; these are summarized in Ref. 3.5]. The fourth effect, secondary flows, is the area in which our current efforts are primarily focused. We are also continuing our investigations in the area of turbulence suppression by magnetic fields, including the effect of secondary flows on turbulence intensity profiles.

The physical mechanism for secondary flow in a confined plasma flow with a transverse magnetic field is illustrated in Figure 3.1 For simplicity we illustrate a distribution of the Hall current, $J_x(z)$, which one would expect from a first-order analysis. The magnetic field $B=B_z$ is assumed constant. The resulting distribution of the $J \times B$ Lorentz force, acting as a body force against the fluid in the channel cross-plane, then causes a secondary flow field which is characterized by large-scale vortices. It is believed that the presence of this sort of transverse flow-field may have profound implications for the performance of MHD devices [3.6-3.7]. The existence of secondary flow has also been inferred from data obtained at HTGL for temperature profiles, voltage drops and heat transfer [3.8].
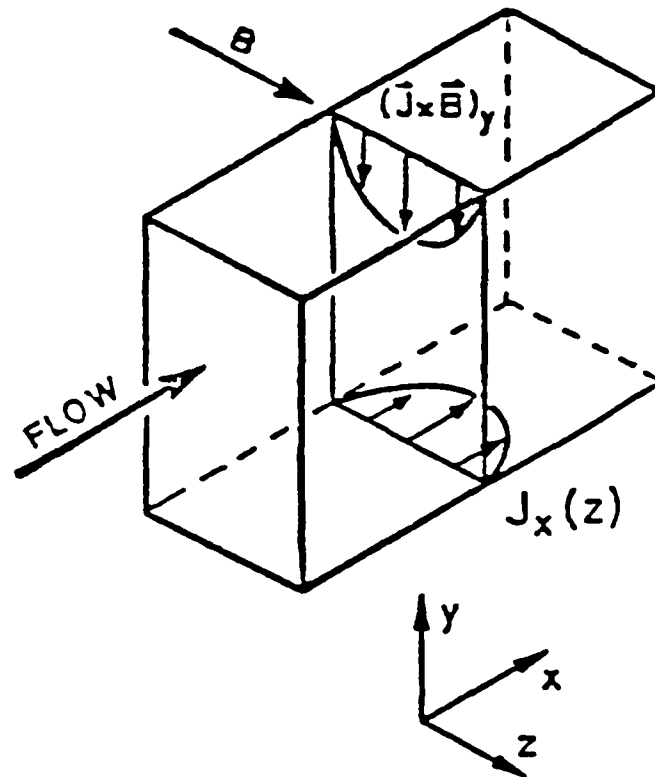
Figure 3.1 Secondary flow mechanism.

Secondary flow and the Hartmann effect are closely related, in that they are both manifestations of the appearance of the Lorentz force in the fluid momentum equation for a collision-dominated plasma,

$$\rho \, \frac{D\mathbf{u}}{Dt} = - \nabla p - \nabla \bar{\bar{\tau}} + \mathbf{J} \times \mathbf{B} \tag{3.1}$$

For a linear MHD device $\mathbf{B}$ is assumed to point in the z-direction; thus the Lorentz force has components in the x- and y-directions. The axial component, $J_y B$, gives rise to the Hartmann effect, while the transverse component, $-J_x B$, causes secondary flow. Whereas the Hartmann effect has been of interest since Hartmann's first investigation, in 1937, it is only recently that secondary flow has received attention.

The presence of fluid turbulence alters in a profound way the transfer of momentum, energy and diffusion in the fluid. Thus, any

model of such a flow must incorporate some, necessarily approximate, representation of turbulent transport. This transport is inherently dependent on the magnitude of the turbulence intensity.

A magnetic field acts to impart Lorentzian forces on the motion of the conducting fluid in general, and on turbulent motion in particular. These forces tend to suppress or damp turbulent components of velocity in the directions perpendicular to the magnetic field. Turbulence damping, and resultant modifications of fluid velocity profiles, are well established for liquid metal flows [3.9]. We have made measurements of the turbulence intensity in partially ionized plasmas [3.4] and have found a similar but quantitatively different behavior. These results demonstrated that the turbulence intensity can be reduced by approximately a factor of two for the moderate values of magnetic interaction achievable in a continuous combustion MHD device. However, it is not yet clear to what extent this turbulence suppression influences profiles of mean axial velocity.

The problem of predicting profiles of mean axial velocity and of turbulence intensity is made more complicated by the presence of discharge-induced secondary flows. In the absence of secondary flows the effects of a magnetic field on turbulence intensity and mean velocity profiles are distributed symmetrically over the channel cross-plane. The large vortex structures characteristic of secondary flow may cause a convective distortion of these profiles. For example, the secondary flow field depicted in Figure 3.1 could sweep slow-moving, turbulent fluid into the top-wall boundary layer while pushing fast-moving, less turbulent core fluid downward toward the bottom wall.

Furthermore, the effects of electromagnetic forces on turbulence in an MHD device may cause the turbulence to become significantly anisotropic, because Lorentz forces do not act along m   tic field lines. The extent and distribution of such anisotropies are im, rtant factors in turbulent transport. This is a phenomenon which has received little experimental attention.

Research Objectives

The over-riding goal of our work in this area is to obtain experimental information which will allow us to describe the three-dimensional flow field in an MHD device. Specifically, the major objectives which presently guide this work are the following:

(1) To study the effect of electromagnetic body forces on the secondary flow field. What are the magnitudes of these secondary flows, and how is their vortex structure affected by applied magnetic fields and discharges?

(2) To study the effect of MHD interaction on mean axial velocity profiles. Are they affected by turbulence suppression caused by the magnetic field, and to what extent are they distorted by secondary flows?

(3) To study the effect of MHD interaction on turbulence. What is the detailed nature of magnetic field turbulence suppression, including the development of anisotropic turbulence? To what extent are turbulence intensity profiles distorted by secondary flows?

Status of Research

Our experiments on MHD boundary layers and secondary flow have been performed at the Stanford M-2 MHD facility. The flow train, shown in Figure 3.2, consists of a 2-MW$_{th}$ combustor, a large mixing plenum for the combustion products, the active channel, a diffuser, and an exhaust system which includes a scrubber. The active channel is enclosed in a 2.6-T copper-coil magnet. The top and bottom walls of the channel can be fitted with up to thirteen pairs of electrodes. These are connected externally through load resistances, and can be configured by means of a patch panel so that various voltages are applied by means of a bank of automobile batteries. This allows us both to achieve higher levels of magnetic interaction and to gain external control of MHD forces.

- 43 -

As our experiments on secondary flow were to be the first such measurements in an MHD channel, it was desirable to design experimental conditions which were as simple and well-controlled as feasible. The most straightforward situation is the one suggested in Figure 3.1, in which the net Hall current is non-zero. Therefore a pair of electrodes at the upstream end of the channel was connected externally to a pair at the downstream end, as shown in Figure 3.3. The magnetic interaction was then maximized by driving a relatively large Hall current down the length of the channel and by operating at a low flowrate.
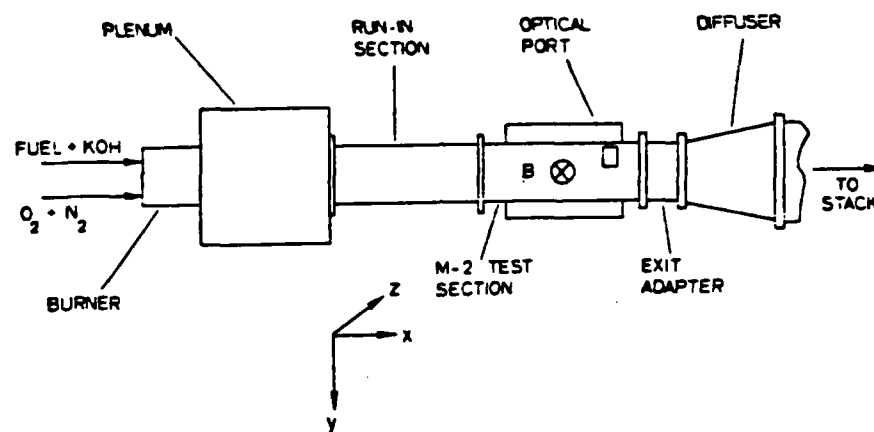
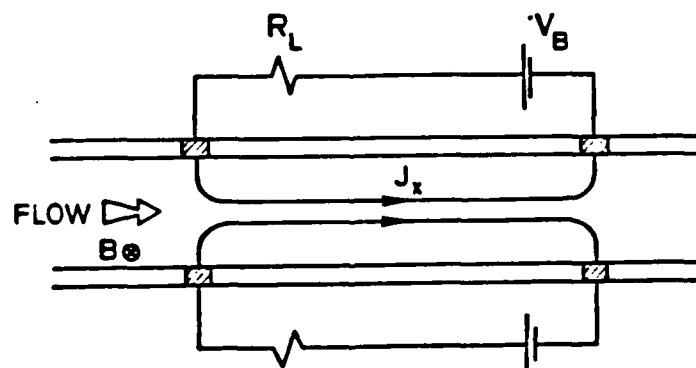Figure 3.2   M-2 facility flow train.

Figure 3.3   Electrical configuration for the secondary flow experiments.

Laser Doppler anemometry was used to measure plasma velocities in both the x- and y-directions. A schematic of the LDA system is shown in Figure 3.4; a more detailed description is found in Ref. 3.10. Essentially, a conventional single-component, dual-beam system was adapted to the particularly difficult circumstances of a combustion MHD flow.

Preliminary measurements of secondary flow, made in 1983, are discussed in Ref. 3.10. These were made under a variety of conditions, but were limited to one quadrant of the channel cross-plane. During the past year we have made more detailed and comprehensive measurements, including measurements of the y-directed velocity component over the entire channel cross-plane. With all other conditions constant, the magnetic induction was varied to produce three cases: (1) B = 2.4 T, pointing in the positive-z direction; (2) B = 2.4 T, pointing in the negative-z direction; and (3) B = 0. The corresponding effect on the J x B body force experienced by the plasma in the cross-plane is that (1) it pointed in the negative-y direction; (2) it pointed in the positive-y direction; and (3) it was zero.

Figure 3.5 shows the results for the positive-B case. The picture here appears immediately to confirm that Lorentz forces strongly affect the transverse flow field. The most significant qualitative feature of the flow field is the degree to which it conforms to the first-order model of Figure 3.1: the top part of the cross-plane is characterized by two large, counter-rotating vortices, which in the core follow the negative-y direction of the Lorentz force. The bottom of these vortices (where the secondary flow is directed in the z-direction, and hence the y-component is zero) is located at Y/H ≅ 0.3. The peak measured velocity had a value 12% of the bulk axial velocity. This velocity evidently peaks quite close to the sidewall, so that the actual maximum was undoubtedly larger than this; in the negative-B case, in which measurements were made closer to the sidewall, the maximum measured value was 14%. The region near the bottom wall does not appear to be characterized by a vortex rotation, but rather by a lifting of the flow away from the wall. This behavior is not predicted by the first-order model, and warrants further study.
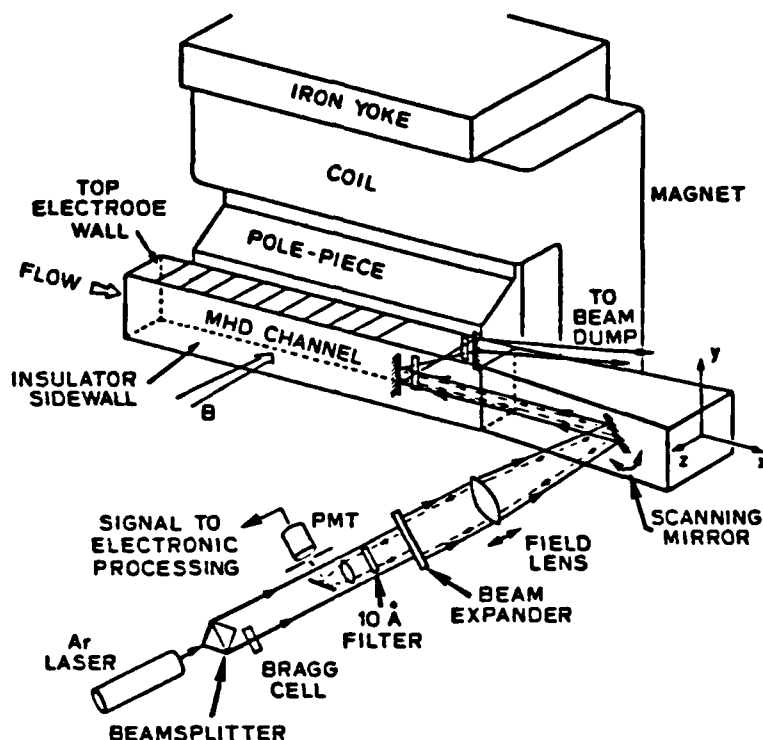
Figure 3.4 Laser doppler anemometry system.

Measurements made on completely separate occasions (but under the same operating conditions) have shown that the data were quite reproducible. Furthermore, measurements made in the negative-B case showed the same results, but rotated by 180° about the channel axis; this is precisely what we expect, as reversing the z-direction of the magnetic field reverses the sign of the y-component of the Lorentz force. Finally, the zero-B results showed a much weaker secondary flow field, with peak velocities 5% of the bulk velocity, and without the two-cell structure of the B-field cases. Taking the results for the three cases together, the evidence appears quite strong that Lorentz forces can exert a definite and strong influence on the secondary flow field in an MHD channel.

We would expect the presence of such a strong secondary flow to have major effects on the plasma thermal and momentum behavior. For example,

- 46 -

the vortices seen in Figure 3.5 would sweep relatively cold sidewall fluid into the top wall boundary layer while pushing hot core fluid downward toward the bottom wall. Preliminary inspection of the data for the three cases appears to demonstrate that this convective effect of secondary flow does indeed cause a redistribution of the transverse profiles of axial mean velocity and turbulence intensity.
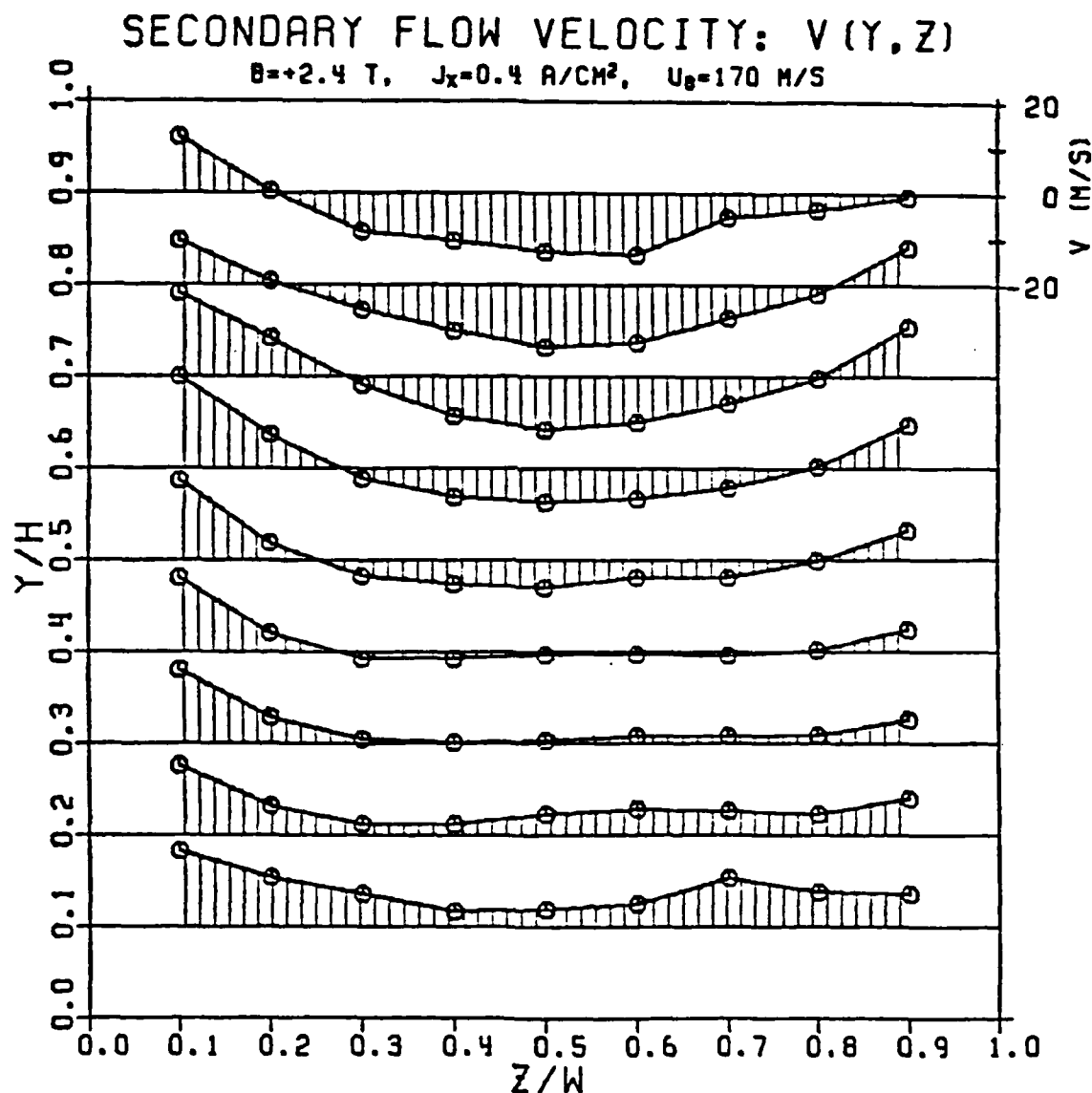

Figure 3.5 Measurements of the y-directed velocity component in the positive-B case.

Figure 3.6 shows measured mean axial velocities as a function of y along the z-centerline. The skewing of the profiles in the B-field cases is quite pronounced. Extending these measurements to the y-z cross-plane, an array of data for the positive-B case yields the isovel graph shown in Figure 3.7. We see that peak axial velocities are pushed downward toward the bottom wall, while slow-moving fluid is swept over the center of the top-wall boundary layer and then pushed downward.

If the fluid being swept from the sidewall into the top wall boundary layer (positive-B case) is cold and electrically resistive, it is also relatively dense, slow and turbulent. Again, our preliminary analysis of measurements, with conditions corresponding to the three secondary flow cases, supports our expectations in this regard. Our data indicate that the region of minimum freestream turbulence is shifted downward from the center of the cross-plane toward the bottom wall; its location corresponds quite closely to the shifted location of the axial velocity peak.

In conclusion, the past year has been one of significant achievement for our program in MHD-induced secondary flow. Previous to this program MHD secondary flow was merely a prediction. Our experimental results are showing that this is indeed a significant phenomenon. The data from these experiments are still being analyzed, but it is already evident that several of the effects of secondary flow (on profiles of axial velocity, turbulence intensity and electrical conductivity) have been demonstrated to be quite pronounced.
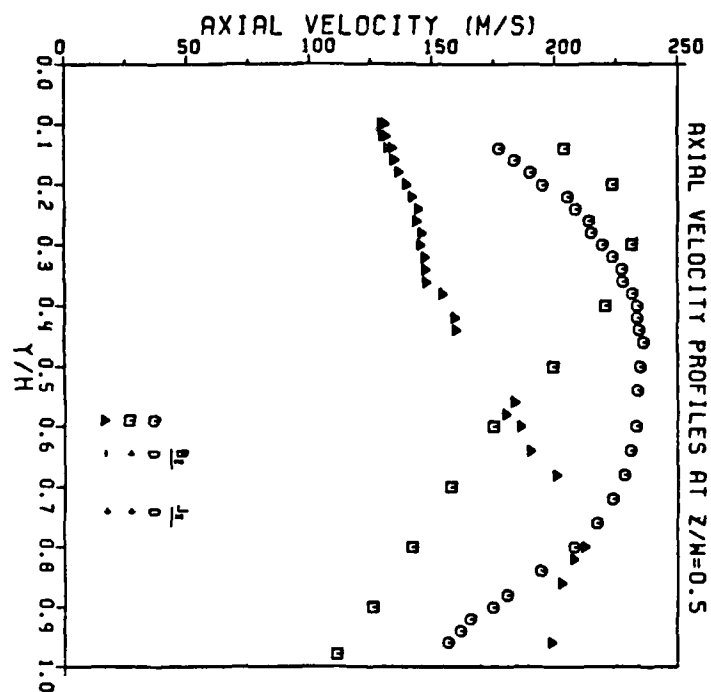
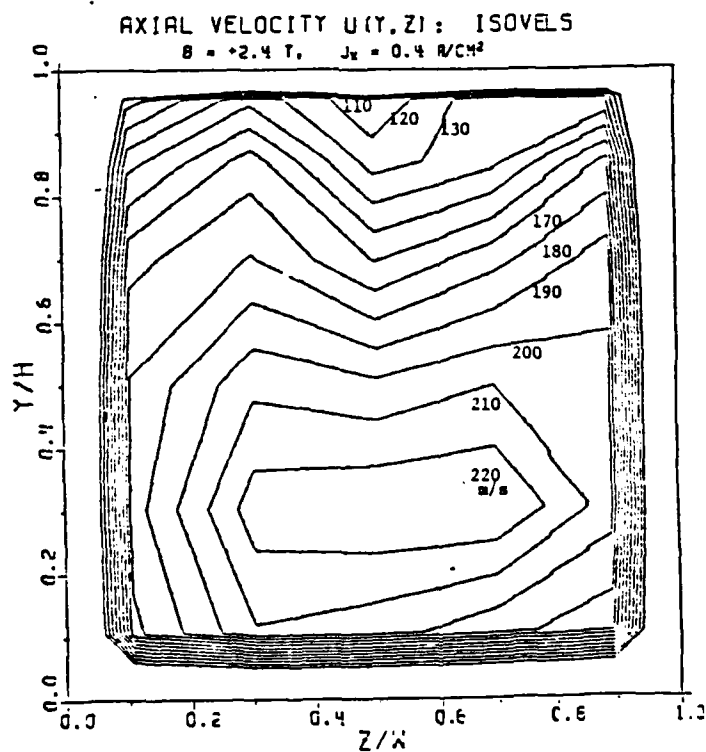Figure 3.6 Effect of secondary flow on mean and velocity profiles.

Figure 3.7 Axial velocity contours based on measurements for the positive-B case.

3.0 REFERENCES

1.1   James, R.K. "Joule Heating Effects in the Electrode Wall Boundary Layer of MHD Generators", HTGL Report No. 115, Stanford University, January 1980.

1.2   Kelley, R., and P.J. Padley, "Measurement of Collisional Ionization Cross-Sections for Metal Atoms in Flames", Proc. Roy. Soc. A-327, p. 345, (1972).

1.3   Bates, D.R., "Ionization and Recombination in Flames", Proc. Roy. Soc. A-348, p. 427, (1976).

1.4   Hinnov, E., and J.G. Hirschberg, "Electron-Ion Recombination in Dense Plasmas", Phys. Rev. 125, p. 795, (1962).

1.5   Bates, D.R., V. Malaviya, and N.A. Young, "Electron-Ion Recombination in a Dense Molecular Gas", Proc. Roy. Soc., A-320, p. 437, (1971).

1.6   Mitchner, M., and C.H. Kruger, Partially Ionized Gases, John Wiley, 1973, p. 146.

1.7   Ibid, p. 32.

1.8   Ibid, p. 52.

1.9   Marr, G.V., Photoionization Processes in Gases, Acdademic Press, 19 , 1967, p. 236.

1.10   Herzburg, G., Spectra of Diatomic Molecules, Van Nostrand Reinhold, 1950, p.449.

1.11   Welty et al., Fundamentals of Momentum, Heat, and Mass Transfer, 1976, p.566.

1.12   Nygaard, K.J., "On the Effect of Cs in Photoionization Laser Plasmas", IEEE J. Quantum Electronics, QE-9, P1020.

1.13   Trenholme, J.B., and J.L. Emmett, "Ultraviolet Output from Pulsed Short Arcs", Naval Research Lab, NRL-NR-2427, 1972.

1.14   Hodgson, B.W., and J.P. Keene, "Sone Characteristics of a Pulsed Xe Lamp", Rev. Sc. Instr., 43, p.493, (1972).

1.15   Hower, N.L., "Measurements of Electrical Conductivity of MHD Plasmas with Four-Pin Probes", Stanford HTGL Scientific Report No. 108, Februrary 1978.

1.16   Houben, J.W.M.A., "Loss Mechanisms in a MHD Generator", Thesis Eidhoven UNiv. of Tech., (1973).

1.17 Borghi, C.A., "Discharges in the Inlet Region of a Noble Gas MHD Generator", Thesis Eindhoven Univ. of Tech., (1982).

2.1 Hirsh, M. N. and Oskam, H. J., eds., Gaseous Electronics, Volume 1: Electrical Discharges, Academic Press, 1978, pp. 291-398.

2.2 Hernburg, Rolf, "Boundary Layer Breakdown and Discharges on Copper Cathodes in a Partially Ionized Molecular Gas", PhD Thesis, Tampere University of Technology, 1983.

2.3 Self, S. A. and Eskin, L. D., "The Boundary Layer Between Electrodes and a Thermal Plasma", IEEE Trans. Plasma Science, Vol. PS-11, pp. 279-285 (Dec 1983).

3.1 James, R. K. and Kruger, C. H., "Joule Heating Effects in the Electrode Wall Boundary Layer of MHD Generators," AIAA J., 21, 679 (1983).

3.2 Rankin, R. R., Self, S. A. and Eustis, R. H., "Study of the Insulating Wall Boundary Layer in a Faraday MHD Generator, AIAA J., 18, 1094 (1980).

3.3 Olin, J. G., "Turbulence Suppression in Magnetohydrodynamic Flows," SU-IPR Report No. 85, Department of Mechanical Engineering, Stanford University (1966).

3.4 Reis, J. C., Kruger, C.H. and Self, S. A., "Laser Doppler Velocimetry Measurements of Turbulence Suppression in a Combustion-Driven MHD Generator", in Engineering Applications of Laser Velocimetry, edited by H. W. Coleman and P. A. Pfund, New York, American Society of Mechanical Engineers, 49 (1982); accepted for publication in J. Fluid Mech.

3.5 Kruger, C. H. and Girshick, S. L., "A Review of MHD Boundary Layer Research at Stanford, with Emphasis on Measurements of the Effects of Secondary Flows," 8th International Conference on MHD Electrical Power Generation, Moscow, USSR, September 1983.

3.6 Doss, E. D. and Ahluwalia, R. K., "Three-Dimensional Flow Development in MHD Generators at Part Load," J. Energy, 7, 289 (1983); AIAA Paper 82-0324 (1982).

3.7 Maxwell, C. D., et. al, "Three-Dimensional Effects in Large Scale MHD Generators," AIAA 14th Fluid and Plasma Dynamics Conference, Palo Alto, California, June 1981 (AIAA-81-1231).

3.8 Girshick, S. L. and Kruger, C. H., "Evidence of Secondary Flow in Faraday MHD Generators," 21st Symposium on Engineering Aspects of Magnetohydrodynamics, Argonne, Illinois, June 1983.

3.9 Reed, C. B. and Lykoudis, P. S., "The Effect of a Transverse Magnetic Field on Shear Turbulence," J. Fluid Mech., 89, part 1, 147 (1978).

3.10 Girshick, S. L. and Kruger, C. H., "Measurements of Secondary Flow in an MHD Channel," 22nd Symposium on Engineering Aspects of MHD, Mississippi State University, June 1984.

4.0 PUBLICATIONS AND PRESENTATIONS

1. Self, S.A. and L. Eskin, "The Boundary Layers Between Electrodes and a Thermal Plasma," IEEE Trans. Plasma Science, P.S. 11, 279-285 (Dec. 1983).

2. Kruger, C.H. and S.L. Girshick, "A Review of MHD Boundary Layer Research at Stanford, with Emphasis on Measurements of the Effects of Secondary Flows," 8th International Conference on MHD Electrical Power Generation, Moscow, USSR (1983).

3. Girshick, S.L. and C.H. Kruger, "Evidence of Secondary Flow in Faraday MHD Generators," 21st Symposium on Engineering Aspects of Magnetohydrodynamics, Argonne, Illinois (1983).

4. Girshick, S.L. and C.H. Kruger, "The Transverse Flow Field in an MHD Channel," IEEE International Conference on Plasma Science, May 14-16, 1984, St. Louis.

5. Girshick, S.L. and C.H. Kruger, "Measurements of Secondary Flow in an MHD Channel," 22nd Symposium on Engineering Aspects of MHD, Mississippi State University, Mississippi, June 26-28, 1984.

5.0 PERSONNEL

The following personnel contributed to this report.

Charles H. Kruger   Professor and Chairman, Department of Mechanical Engineering (Ph.D. Mechanical Engineering, minor Physics, Massachusetts Institute of Technology 1960. Thesis: "The Axial Flow Compressor in the Free Molecule Range")

Morton Mitchner   Professor, Department of Mechanical Engineering (Ph.D. Physics, Harvard University 1952. Thesis: "The Propagation of Turbulence into a Laminar Boundary Layer")

Sidney A. Self   Professor (Research), Department of Mechanical Engineering (Ph.D. Physics, London University 1965. Thesis: "Radio-Frequency Interaction in a Beam-Generated Plasma System")

Leo D. Eskin   Research Assistant, High Temperature Gasdynamics Laboratory, Department of Mechanical Engineering. (M.S. Mechanical Engineering, Virginia Polytechnic Institute and State University 1981. Thesis: "Application of the Monte Carlo Method to the Transient Thermal Modeling of a Diffuse-Specular Radiometer Cavity")

Stephen M. Jaffe   Research Assistant, High Temperature Gasdynamics Laboratory, Department of Mechanical Engineering (M.S. Mechanical Engineering, Stanford University 1983)

Steven L. Girshick   Research Assistant, High Temperature Gasdynamics Laboratory, Department of Mechanical Engineering (M.S. Mechanical Engineering, Stanford University 1981)

END

FILMED

11-85

DTIC